Search for associations containing young stars (SACY)

VIII. An updated census of spectroscopic binary systems exhibiting hints of non-universal multiplicity among their associations*

S. Zúñiga-Fernández[1,2,3], A. Bayo[3,1], P. Elliott[4], C. Zamora[1,3], G. Corvalán[1,3], X. Haubois[2], J. M. Corral-Santana[2], J. Olofsson[3,1], N. Huélamo[5], M. F. Sterzik[7], C. A. O. Torres[6], G. R. Quast[6], and C. H. F. Melo[2]

[1] Núcleo Milenio de Formación Planetaria (NPF), Valparaíso, Chile
    e-mail: sebastian.zuniga@postgrado.uv.cl
[2] European Southern Observatory, Alonso de Córdova 3107, Vitacura, Casilla 19001, Santiago de Chile, Chile
[3] Universidad de Valparaíso, Instituto de Física y Astronomía (IFA), Avenida Gran Bretaña 1111, Casilla 5030, Valparaíso, Chile
[4] Department of Physics and Astronomy, York University, Toronto ON M3J 1P3, Canada
[5] Centro de Astrobiología (CSIC-INTA), ESAC Campus, Camino del Castillo s/n, 28692 Villanueva de la Cañada, Madrid, Spain
[6] Laboratório Nacional de Astrofísica/MCTIC, Rua Estados Unidos 154, 37504-364 Itajubá, MG, Brazil
[7] European Southern Observatory, Karl-Schwarzschild-Str. 2, 85748 Garching bei Munchen, Germany

ABSTRACT

Context. Nearby young associations offer one of the best opportunities for a detailed study of the properties of young stellar and substellar objects thanks to their proximity (<200 pc) and age ($\sim 5-150$ Myr). Previous works have identified spectroscopic (<5 au) binaries, close ($5-1000$ au) visual binaries, and wide or extremely wide ($1000-100\,000$ au) binaries in the young associations. In most of the previous analyses, single-lined spectroscopic binaries (SB1) were identified based on radial velocities variations. However, this apparent variation may also be caused by mechanisms unrelated to multiplicity.
Aims. We seek to update the spectroscopy binary fraction of the Search for Associations Containing Young stars (SACY) sample, taking into consideration all possible biases in our identification of binary candidates, such as activity and rotation.
Methods. Using high-resolution spectroscopic observations, we produced ~ 1300 cross-correlation functions (CCFs) to disentangle the previously mentioned sources of contamination. The radial velocity values we obtained were cross-matched with the literature and then used to revise and update the spectroscopic binary (SB) fraction in each object of the SACY association. In order to better describe the CCF profile, we calculated a set of high-order cross-correlation features to determine the origin of the variations in radial velocities.
Results. We identified 68 SB candidates from our sample of 410 objects. Our results hint that at the possibility that the youngest associations have a higher SB fraction. Specifically, we found sensitivity-corrected SB fractions of $22^{+15}_{-11}\%$ for ϵ Cha , $31^{+16}_{-14}\%$ for TW Hya and $32^{+9}_{-8}\%$ for β Pictoris, in contrast to the five oldest associations we have sampled ($\sim 35-125$ Myr) which are $\sim 10\%$ or lower. This result seems independent of the methodology used to asses membership to the associations.
Conclusions. The new CCF analysis, radial velocity estimates, and SB candidates are particularly relevant for membership revision of targets in young stellar associations. These targets would be ideal candidates for follow-up campaigns using high-resolution techniques to confirm binarity, resolve orbits, and, ideally, calculate dynamical masses. Additionally, if the results on the SB fraction in the youngest associations were confirmed, it could hint at a non-universal multiplicity among SACY associations.

Key words. binaries: spectroscopic – stars: pre-main sequence – stars: formation – techniques: radial velocities – techniques: spectroscopic

1. Introduction

Ever since the first nearby young moving group of stars was identified around 30 years ago (TW Hya association, de la Reza et al. 1989; Kastner et al. 1997), extensive research has been dedicated to these stellar associations – from identifying new ones and their members to characterising their chemical composition, dynamics, ages, and multiplicity fractions (see Zuckerman et al. 2004; Torres et al. 2008; Shkolnik et al. 2012; Malo et al. 2014; Elliott & Bayo 2016; Gagné et al. 2018, among others). These nearby populations, given their age ($\sim 5-150$ Myr) and proximity

(<200 pc), are great laboratories for the study of the properties of young stellar and substellar objects.

Recent studies have used youth signatures (such as the presence of Hα in emission or the detection of the Li λ 6707 Å line) and 6D kinematics (i.e. Galactic position and Galactic velocity in the six-parameter space, XYZ and UVW) to estimate membership (Schneider et al. 2019; Lee & Song 2019). In this context, multiplicity studies (particularly the search for tight binaries) play an important role since age diagnostics, velocity determinations, and astrometry are often affected by the application of single-star models to blended multiple systems.

More generally speaking, stellar multiplicity is important in a broad range of fields (e.g. supernova rates), however, here we focus on its impact on the star-formation processes. Works on

---

* Full Tables G.1, G.2, and G.4 are only available at the CDS via anonymous ftp to cdsarc.u-strasbg.fr (130.79.128.5) or via http://cdsarc.u-strasbg.fr/viz-bin/cat/J/A+A/645/A30

multiplicity as a function of environment, along with detailed studies of composition and orbital parameters, provide valuable empirical data that improve our understanding of stellar evolution and unresolved stellar populations. These empirical estimates are of particular interest at younger ages and close separations, where theoretical models still remain only loosely constrained (Duchêne et al. 2007; Connelley et al. 2008; Tobin et al. 2016) and the literature in this field is still lacking in comparison to the more exhaustive work done for main-sequence (MS) stars with volume-limited samples (Tokovinin 2014a, 2019; Tokovinin & Briceno 2020; Sperauskas et al. 2019; Merle et al. 2020).

It is widely accepted that almost half of solar-type stars spend their time in the MS as multiple systems (Tokovinin 2014a; Raghavan et al. 2010). There is also growing evidence that multiplicity is even higher at very young ages (Tobin et al. 2016), possibly indicating the primordial nature of multiplicity in the processes of star formation. Observational studies suggest an overall decrease of the binary fraction from pre-MS ages to field ages (Ghez et al. 1997; Kouwenhoven et al. 2007; Raghavan et al. 2010). This decrease could be a consequence of disruption process in long-period systems due to interactions with other systems (Raghavan et al. 2010) or due to the dynamical evolution of wide companions in triple or higher order systems (Sterzik & Tokovinin 2002; Reipurth & Mikkola 2012; Elliott & Bayo 2016). In contrast with wide binaries, tight binaries are expected to "last" longer given their larger binding energy. A number of observational results on tight binaries have indicated that the overall SB fraction remains unchanged after 1 Myr (Nguyen et al. 2012; Tokovinin 2014b; Elliott et al. 2014). However, more recently, Jaehnig et al. (2017) suggested that some SBs (periods $\approx 10^2 - 10^4$ days) in pre-MS clusters ($\approx 1 - 10$ Myr) can be dynamical disrupted prior to reaching the MS. The evolution and the formation channel of multiple stellar systems cannot be easily determined by field stars, where billions of years of dynamical evolution have already occurred. Therefore, it is necessary to devote specific studies of the stellar multiplicity from star-forming regions (SFRs) to the young associations ($1 - 100$ Myr).

The multiplicity studies for the youngest stars (≤ 100 Myr) are still dominated by low number statistics. This is particularly critical in the case of SBs (sub-au separation scales) where high-resolution techniques are mandatory (Melo 2003; Nguyen et al. 2012; Viana Almeida et al. 2012), but some of these techniques can be contaminated by phenomena such as activity and rotation, inherent to the young ages involved (see Sect. 5). In principle, the preferred mechanism to form some of these close binaries ($\lesssim 100$ au) is disk fragmentation, where the disk fragments as a result of gravitational instabilities (Bonnell & Bate 1994; Zhu et al. 2012). However, the formation mechanisms could be affected by environment conditions. In particular, Bate (2019) found an apparent trend for multiple systems to be preferentially tighter when formed at lower metallicity environments. On the other hand, the tightest systems ($\lesssim 10$ au) can neither form directly via turbulent nor disk fragmentation, and the emerging consensus is that some processing must dynamically evolve the initial separations to closer ones (Bate et al. 2002). In particular, Tokovinin et al. (2006) found that ~63% of MS SBs were members of high-order multiple systems (see Elliott & Bayo 2016 for a similar result focused on the β Pictoris moving group). Interestingly, ~98% of SBs with orbital periods shorter than three days have additional companions. This result seems to provide observational support to the dynamical evolution hypothesis commented above. Further SB studies in younger population

(≤ 100 Myr) are, in any case, still needed to provide improved statistics on more pristine populations.

This work is the continuation of a series of studies of multiplicity in young associations over a wide range of orbital parameters ($a \sim 0.1 - 10^4$ au: Elliott et al. 2014, 2015, 2016; Elliott & Bayo 2016). In particular, this work focuses on SB identification within SACY via cross-correlation function (CCF), not only using the radial velocity (RV) variations with time as a sign of multiplicity, but also incorporating high-order features as a complementary tool to establish the origin of the variation. Following our modelling and upon applying observational bias corrections, we present the results on the SB fraction in each association within the SACY sample along with the list of SB candidates, including notes on individual objects.

2. Sample

The sample presented in this work is drawn from our database of young association members, as in Elliott et al. (2016), mainly gathered from Torres et al. (2006, 2008), Zuckerman et al. (2011), Malo et al. (2014), Kraus et al. (2014), Elliott et al. (2014), and Murphy et al. (2015). The membership of each object to a given association was assessed using the convergence method described in Torres et al. (2006) and Torres et al. (2008) with the updated distances from the second *Gaia* data release (*Gaia* DR2, Gaia Collaboration 2018). The full membership study and further analysis will be presented in Torres et al. (in prep.). In addition, the targets selected for this work have to fulfil at least one of the following selection criteria: 1. The objects have at least one high-resolution spectrum in our database from which a CCF can be calculated; 2. The target has at least one RV measurement (with uncertainty ≤ 3 km s^{-1}) and one $v \sin i$ value given in the literature (with uncertainty ≤ 5 km s^{-1}).

Hereafter, this selection is referred as "the sample" and obtained with the SACY convergence method unless otherwise indicated. Our sample covers an approximate mass range of $0.1 - 1.5 \, M_\odot$, with the majority of objects having an estimated mass around $1 \, M_\odot$. Masses were estimated from the 2MASS near-infrared magnitudes and parallactic distances using the evolutionary tracks from Baraffe et al. (2015). Our final sample size is 410 objects, 303 of which have two or more epochs of high-resolution spectra. Further details on the literature measurements used in our sample are summarised in Sect. 3.2, and all relevant parameters for this work are listed in Table G.4.

3. Observations and additional data

We obtained spectra taken with the Ultraviolet and Visual Echelle Spectrograph (UVES; $\lambda/\Delta\lambda \sim 40\,000$ with a 1″ slit, Dekker et al. 2000) in Paranal, Chile. These observations came from three of our observing campaigns, taken between 2015 and 2016. We also added data retrieved from the ESO phase 3 public archive[1]. Our data were taken with a 1″ slit width in the wavelength range 3250−6800 Å. The time separation between different observing epochs of a given source ranges from one day to ~one month.

The data were reduced with the EsoRex[2] pipeline of UVES, using the *uves_obs_redchain* recipe (bias corrected, dark-current-corrected, flat-fielded, wavelength-calibrated and extracted). This provides three spectra from the two arms of the instrument (BLUE and REDL/REDU, with wavelength coverage

3250−4500 Å, 4800−5800 Å, and 5800−6800 Å, respectively). For the calculation of CCF in this work, we combined all three spectra in the case where the average signal-to-noise ratio (S/N) for the BLUE spectrum is >10. Otherwise, we combined the REDU and REDL spectra only. In total, we present 998 individual CCFs from the UVES observations.

3.1. Archival high-resolution spectra

In order to maximise the time baseline and available spectral information for each target, we used the publicly available phase 3 data taken with the Fibre-fed Extended Range Échelle Spectrograph (FEROS/2.2 m, Kaufer et al. 1999) and the High Accuracy Radial velocity Planet Searcher (HARPS/3.6 m, Mayor et al. 2003).

FEROS is a high-resolution Échelle spectrograph ($\lambda/\Delta\lambda \approx$ 50 000) installed at the MPG/ESO 2.2-m telescope located at ESO's La Silla Observatory, Chile. The wavelength range of the reduced spectra is 3527−9217 Å. The one dimensional Phase 3 spectra are given in the barycentric reference frame. HARPS is also a high-resolution Échelle spectrograph ($\lambda/\Delta\lambda \approx$ 115 000), mounted on the 3.6 m telescope, also located at La Silla Observatory in Chile. The wavelength range is 3781−6912 Å and the phase 3 spectra are given in the barycentric reference frame.

We searched for any available science spectra for targets in common with our database of young moving group members. From all the archival spectra, we successfully calculated CCFs for 167 observations taken with FEROS and 97 CCFs for observations taken with HARPS. These data are also included in the analysis presented in this work.

3.2. Previously published quantities

Table 1 lists the references used in this work for both the RV and $v \sin i$ values. As mentioned previously, we only include values that have uncertainties ≤3 km s^{-1} and ≤5 km s^{-1} for RV and $v \sin i$, respectively. The table is split into two sections: the top one shows values that do not have associated Modified Julian Dates (MJD) values for each RV and the bottom section corresponds to surveys that do have individual MJD values for each observation.

3.3. Gaia Data Release 2

The second *Gaia* data release[3] (hereafter, *Gaia* DR2) was issued on 25 April 2018, providing accurate proper motions and parallaxes (among other astrophysical parameters) for more than a billion sources. In particular, this *Gaia* data release also includes for the first time RV values (Katz et al. 2018) for objects with a mean G magnitude between ~4 and ~13 and effective temperatures ($T_{\rm eff}$) between 3550 and 6900 K. The overall precision of the RV at the bright-end is in the order of 200−300 m s^{-1}, while at the faint-end, it deteriorates to ~1.2 km s^{-1} for a $T_{\rm eff}$ of 4750 K and ~2.5 km s^{-1} for a $T_{\rm eff}$ of 6500 K. Stars identified as double-lined spectroscopic binaries are not reported in *Gaia* DR2, whereas variable single-lined, variable star, and non-detected double-lined spectroscopic binaries have been treated as single stars in the same release (Sartoretti et al. 2018).

Table 1. Previous catalogues of RV and $v \sin i$ values used in this work.

Refs.	Values	MJD-range	Ref. code
MJD estimated from observation range			
Schlieder et al. (2012)	RV, $v \sin i$	54718–55685	SC12
Shkolnik et al. (2012)	RV [a]	53725–54455	SH12
Torres et al. (2006)	RV, $v \sin i$	51179–53826	TO06
Lopez-Santiago et al. (2006)	RV [b]	51910–52796	LO06
Rodriguez et al. (2013)	RV	56171–56230	RO13
Maldonado et al. (2010)	RV	53552–54771	MA10
Moór et al. (2013)	RV	55013–55669	MO13
Reiners & Basri (2009)	RV	54475–54835	RE09
Gontcharov (2006)	RV	47892–52275	GO06
Exact MJD values available for each observation			
Malo et al. (2014)	RV, $v \sin i$	54996–56532	MA14
Kraus et al. (2014)	RV [c]	56124–56327	KR14
Montes et al. (2001)	RV	51384–51566	MO01b
Mochnacki et al. (2002)	RV	51082–52003	MO02
Bailey et al. (2012)	RV, $v \sin i$	53327–54963	BA12
Desidera et al. (2015)	RV, $v \sin i$	53102–55399	DE15

Notes. The bottom section shows those values with associated MJDs, while the top section show values for which MJDs have been estimated from the respective MJD-range. [a]Extended from Shkolnik et al. (2010), [b]stars added to the initial sample of Zuckerman et al. (2004), [c]$v \sin i$ values not used from Kraus et al. (2014) as these values are the standard deviation of the broadening function, not calibrated $v \sin i$ values.

We retrieved *Gaia* DR2 data for all the objects in the SACY sample using the `astroquery Vizier` package[4]. We updated our local database to use identifiers resovable by the Sesame service and the *Gaia* DR2 queries were based on those identifiers. Objects not resolved by identifiers were instead searched by coordinates. In both cases we ran an initial query with a 10″ radius and used the proper motions of the closest *Gaia* source, within the radius, to derive its J2000 coordinates (that are those originally included in our local database). Those J2000 coordinates were then matched to the coordinates in our local database with a 1″ radius. Objects outside of this 1″ radius were individually inspected (see Fig. E.1) by cross validating using Simbad, Vizier and the TESS input catalogue (TIC-8, Stassun et al. 2019). We recovered *Gaia* DR2 counterparts for 805 out of 837 targets in our local database, corresponding to a completeness of 96.2% (see Fig. 1). From these 805 objects, 374 have RV measurements from *Gaia*, which were used in this work as an additional epoch of data. Our database comprises 2379 RV measurements and 1515 $v \sin i$ values, 1151 of which come from our CCF calculation of high-resolution spectra. All these values, together with other additional properties, can be found in Tables G.1 and G.2.

3.4. Assessing membership using BANYAN Σ

In order to asses any possible bias throughout this work with the use of the convergence method to build the census of the different associations, we followed an independent path, utilising the BANYAN Σ tool[5] for young association membership.

---

[3] https://www.cosmos.esa.int/web/gaia/dr2

[4] https://astroquery.readthedocs.io/en/latest/vizier/vizier.html

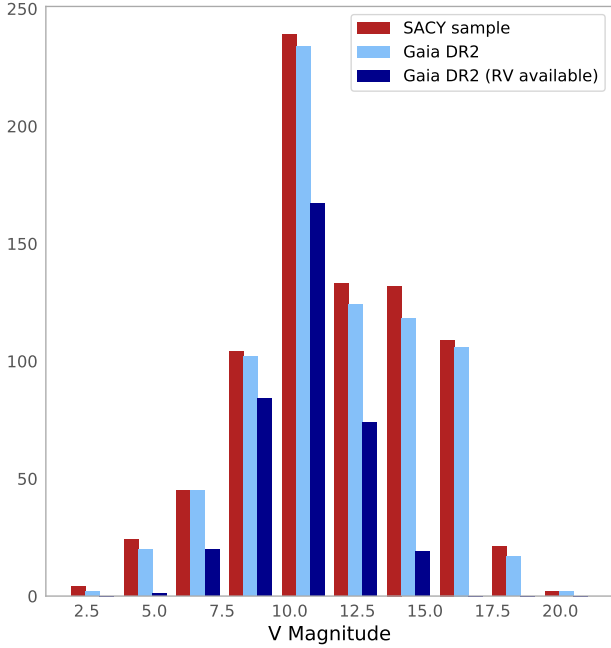[5] https://github.com/jgagneastro/banyan_sigma

Fig. 1. *V*-magnitude distribution of all members of the SACY sample along with those with a counterpart in the *Gaia* DR2. We reach a completeness of 96.2%, where 44.7% of the objects count based on a *Gaia* RV estimate.

Fig. 2. *Top*: number of targets belonging to each young associations identified by our convergence method (SACY) and BANYAN Σ. *Bottom*: mass function of the census built with the convergence method and BANYAN Σ for membership assessment.

Accurate RV, distances, and proper motion values are key ingredients in the accuracy of our convergence method (Torres et al. 2006, 2008). Similarly, the recovery rate of BANYAN Σ is 68% when proper motion and RV are used and 90% when parallaxes are included (Gagné et al. 2018). Therefore, as we did for the convergence method, we fed the RV measurements collected in this work plus the *Gaia* DR2 proper motion and parallaxes to the BANYAN Σ tool for membership assessment.

It is out of the scope of this work to develop or establish a metric to compare in detail the outcome of the two methodologies. However, the two resulting censuses allow us to test the robustness of our results against moderate changes in membership (see Sect. 8 for further details). The membership results for the SACY convergence method and BANYAN Σ are available in Table G.4 and summarised in Fig. 2. The mass distributions of the samples analysed throughout this work (using either our convergence method or BANYAN Σ tool) are shown in the bottom panel of Fig. 2. As it can be seen, the only associations with noticeable differences regarding total number of members are ABD and THA.

3.5. Rotational periods from light curves

In order to estimate the rotational periods of the objects in the sample, we queried two of the main missions delivering precise light curves: K2 and TESS (Howell et al. 2014; Ricker et al. 2015). We began by querying the archives of both missions via the MAST API (via the `astroquery` package within `astropy`) with the J2000 coordinates of each object and a search radius of 0.002 deg (∼7″). We obtained light curves for 272 out of 410 objects (∼65% of the sample). In particular, 266 were taken with TESS (across different sectors) and six with K2. In all cases, we chose the Pre-search Data Conditioned Simple Aperture Photometry (PCDSAP) fluxes and characterised the variability of
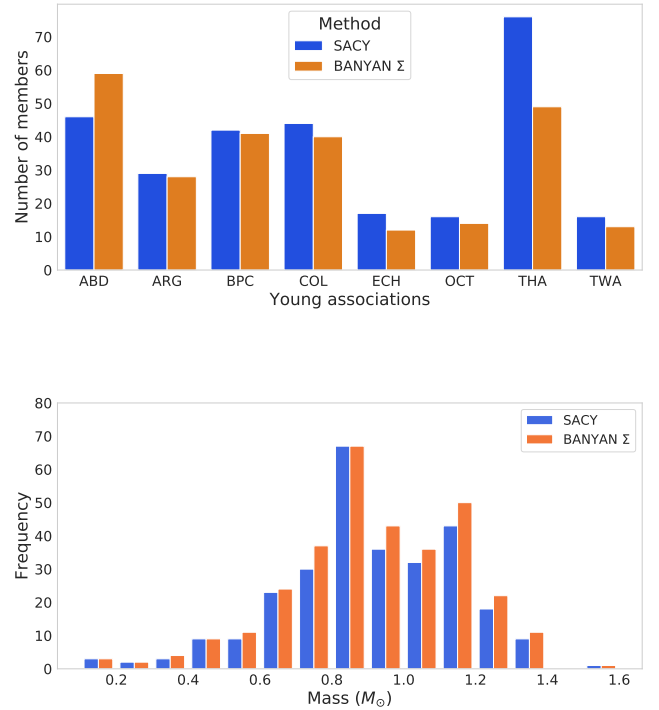
the sources via their Lomb-Scargle (LS) periodograms (calculated with `astropy.timeseries.lombscargle`, VanderPlas & Ivezic 2015).

Even though the false alarm probabilities (FAPs) of the peaks identified in the LS periodogram were extremely low (typically well below 10^{-4}), we performed a simple quality check for the identified periods in the following way: we folded each light curve to the period with the highest intensity in the LS periodogram and modelled the modulation by calculating the median, binning the phased curve in 100 bins. Such a trend was subtracted from the phased light curve and the median absolute deviation (MAD) of those residuals was compared to the MAD of the original phased light curve.

In the case of TESS data, additional checks need to be done to account for the large pixel size of its detector. In order to estimate the contamination that could affect each of the light curves, we modified the existing python package `tpfplotter` (Aller et al. 2020) which, in short, provides the number of *Gaia* sources within a ΔG mag (*Gaia* G mag, this Δ is defined by the user) of the science target that fall in the pipeline aperture of TESS. We modified the code in order to take into account both the proper motions of our targets and the cross-match with *Gaia* DR2 (explained in Sect. 3.3). We chose a ΔG mag on the order of five magnitudes and in Table G.4, we include notes on the minimum ΔG mag found within the aperture. We note that a number (27 to be precise) of our *Gaia* cross-match identifications are not recovered in Simbad. Even though we stand by those identifications, we make note of them in the column *LC notes* of Table G.4.

We classified a period as "good quality" if the MAD of the residuals is at least three times smaller than the MAD of the original phased light curve and if there are no *Gaia* sources that fall in the aperture with ΔG mag < 5. Periods that fulfil the criteria
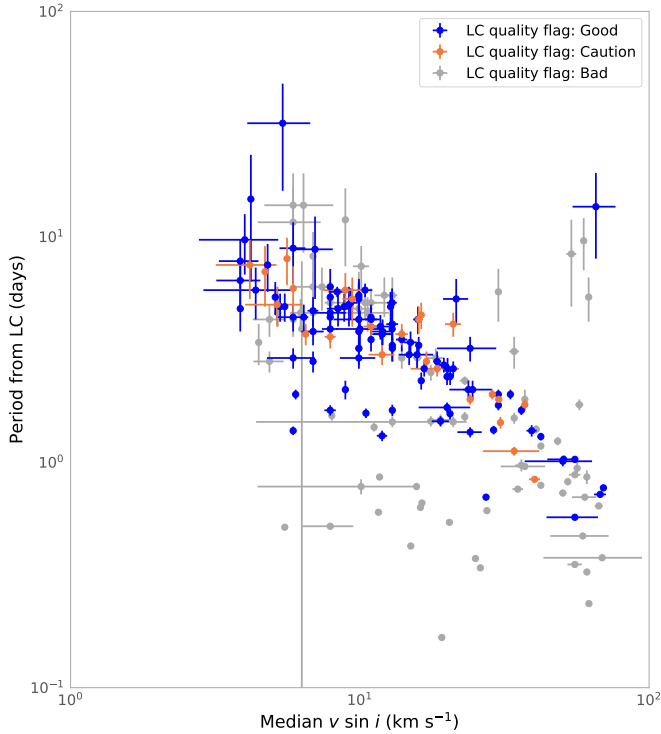
Fig. 3. Rotational periods estimated from the light curves versus median $v \sin i$ from our work. The quality flag of the period defined in Sect. 3.5, is colour-coded as grey, orange, and blue for "bad" caution and "good", respectively.

based on the MAD of the residuals but have contaminants in the aperture with $2.5 \le \Delta G \, \mathrm{mag} \le 5$ should be considered with caution. For periods that present contaminants in the TESS aperture and do not fulfil the criteria based on the MAD are not considered as reliable for the rest of the analysis and are flagged as being of "bad quality". For an example of a clearly contaminated light curve (rotational periods that are not to be trusted) see Appendix F.

Our estimated periods as a function of median $v \sin i$ from our work are presented in Fig. 3 (see the details regarding $v \sin i$ estimation in Appendix. B). This relation was used throughout our analysis as a complementary source to evaluate the nature of SB candidates.

4. Properties and calculation of CCF profiles

There are two main ways of calculating CCFs from high-resolution spectra, using either observations of RV standard stars or a numerical mask acting as a standard star. In this analysis, we used a CORAVEL-type numerical mask which was convoluted with the observed spectrum for each observation (for further details, see Queloz 1995). For the sake of homogeneity and given the relatively narrow range of spectral types in our sample (see Table G.4), we use a single K0 mask in our analysis.

Only in cases where the K0 mask completely failed in the CCF calculation (assessed by the goodness of fit of the Gaussian profile to the CCF), we used other available masks (F0 or M4, depending on the spectral type of the star). However, for consistency, the CCF profiles and respective properties of such objects are not included in the statistical analysis of our measurements.

The CCFs analysis and the SB update presented in this work follows up what was presented by Elliott et al. (2014). However,

we do not only enlarge our database of observations here, but we have also chosen to use a much more detailed approach in calculating the CCFs for each observation; by introducing high-order features of the CCFs, we can distinguish between apparent RV variation caused by poor fitting of the CCF and variation produced by bound companions or stellar activity.

4.1. Sources of uncertainty

The uncertainty in RV calculation using a numerical mask ($\sigma_{\mathrm{meas.}}$) can be derived with the following equation (Baranne et al. 1996):

$$\sigma_{\mathrm{meas.}} = \frac{C(T_{\mathrm{eff}})}{D \times S/N} \frac{1 + 0.2\omega}{3} \, \mathrm{km\,s^{-1}}, \qquad (1)$$

where $C(T_{\mathrm{eff}})$ is a constant that depends on both the spectral type of the star and the mask used, which is typically 0.04; ω is the (noiseless) full width at half maximum (in $\mathrm{km\,s^{-1}}$) of the CCF; D is the (noiseless) relative depth, and S/N is the mean signal-to-noise ratio.

This uncertainty is relevant to one measurement of RV from a single observation and a single instrument. Given the high S/N of our data, typically in the range of ∼50−100, the calculated uncertainty is almost negligible. A more empirical approach can be taken by studying the RV from different epochs and gauging the level of intrinsic variation of the star. As these stars are often variable, the CCF profiles are not always completely symmetric (Lagrange et al. 2013) and, therefore the uncertainty calculated using Eq. (1) is underestimated. Thus, following the analysis presented in Elliott et al. (2014), we use an empirical approach to estimate RV uncertainties (see Sect. 6.1 for further details).

4.2. Cross-correlation features

In order to better describe the CCF profile, we calculate a set of high-order cross-correlation features:

Bisector. The bisector is calculated from the midpoint of the line for each element of intensity that defines the CCF profile. This is shown by the grey dots in upper right panel in Fig. 4.

Bisector inverse slope. Here, we adopt the bisector inverse slope (BIS) as defined by Queloz et al. (2001):

$$BIS = \bar{v}_t - \bar{v}_b, \qquad (2)$$

where $\bar{v}_t$ is the mean bisector velocity in the region between 10% and 40% of the line depth and $\bar{v}_b$ is the mean bisector velocity between 55% and 90% of the line depth. These two regions are highlighted in the bottom right panel of Fig. 4.

Bisector slope (b_b). This is defined as the inverse slope from a linear fit for the region between 25%–80% of the CCF's depth (Dall et al. 2006). This is shown by the red line in the bottom right panel of Fig. 4.

Curvature (c_b). The curvature of the CCF's profile is defined as:

$$c_b = (v_3 - v_2) - (v_2 - v_1) \qquad (3)$$

where v_1, v_2, and v_3 are the mean bisector velocity on the 20–30%, 40–55%, and 75–100% of the CCF's depth. This definition is from Dall et al. (2006) which is a slightly modified version of the curvature presented in Povich et al. (2001).

Anderson-Darling statistic (AD). We use the AD statistic around the peak of the CCF profile as a test for normality, that is,
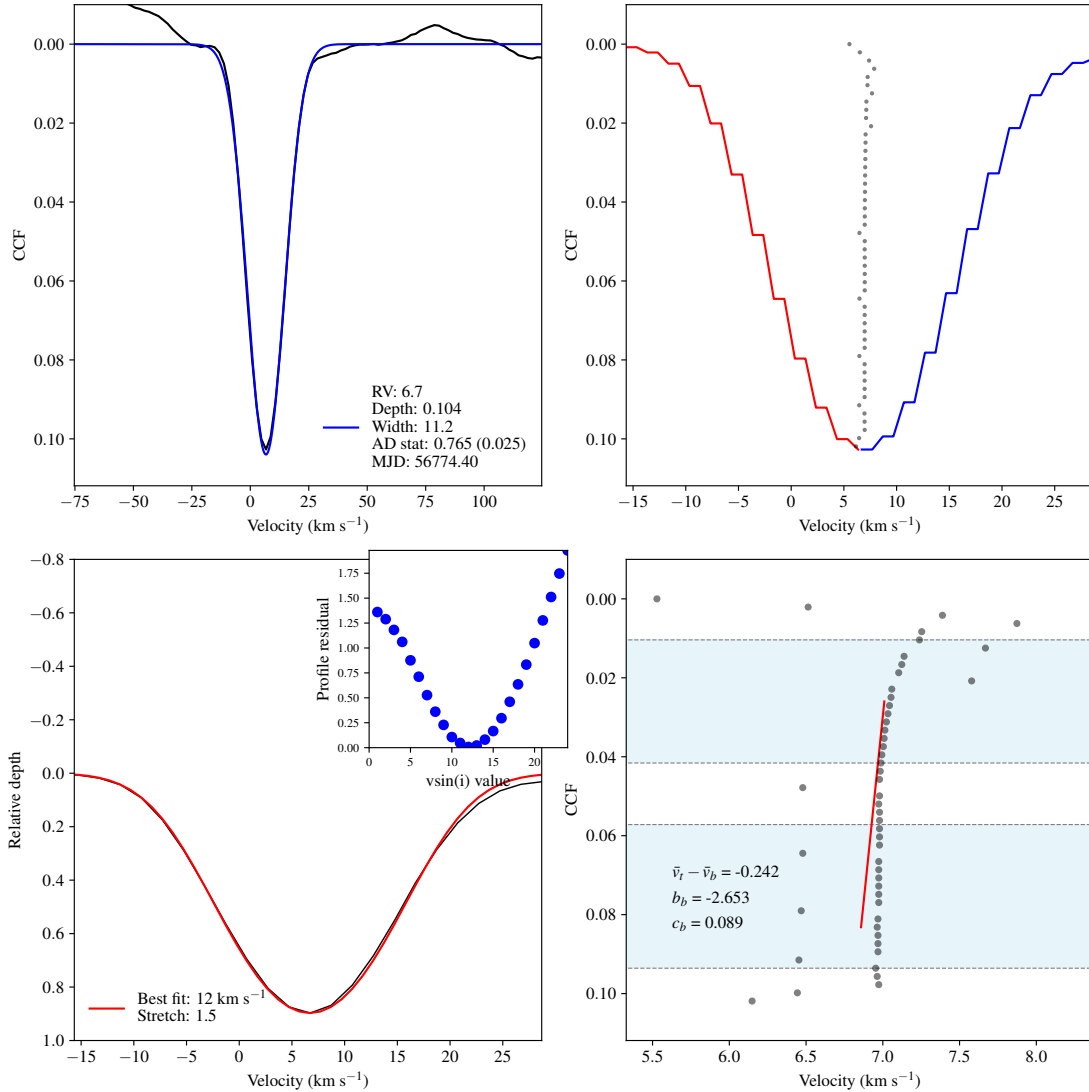
Fig. 4. Example of the graphical output from our CCF calculation code for one target. *Top left*: CCF profile. The quantities shown in the lower left are the peak of the fitted Gaussian profile (RV), the depth of the CCF, the width (σ) of the Gaussian profile, the Anderson-Darling statistic for normality between $-\sigma$ and $+\sigma$ with its respective significance level, and the MJD of the observation. *Top right*: 2σ region of the CCF profile and the bisector (grey dots). *Bottom left*: normalised CCF-fitted with the best-fit rotational profile (from profiles in the $v \sin i$ range 1–200 km s^{-1}). The residuals of fits are shown in the inset. *Bottom right*: bisector slope along with three metrics of its shape (b_b, c_b and *BIS*). See text in Sects. 4 and 5 for further details.

how Gaussian-like the profile is. We perform this test around the 1σ region around the peak of the CCF profile. The AD statistic and its significance are shown in the upper left panel of Fig. 4, that is, the null hypothesis that the function is not Gaussian cannot be rejected at a significant level.

Profile residual. The CCF profile is fitted by a set of rotational profiles (Gray 1976) to determine its $v \sin i$ value. In order to quantify the validity of this fit we calculated the overall residual for each $v \sin i$ profile (from 1 to 200 km s^{-1}). The minimum of this set of residuals is used to determine the best-fit profile for each observation, but also the absolute value is retained. That way, we can compare the absolute residuals as a function of other properties in our sample.

5. Estimates of radial and rotational velocities

To calculate all the properties defined in the previous section from the available high-resolution optical spectra, we wrote a

series of functions[6]. Those functions compute the CCFs and return these properties as a "digest" of the information contained in the CCFs.

Figure 4 shows the summary graphical output from the master function described before. The CCF is shown in the top left panel of Fig. 4, that is, the resulting profile of the star's spectrum with the numerical mask (in black) and the Gaussian profile fitted to the data (in blue). The grey dots in the right panel of Fig. 4 represent the bisector of the profile whereas the red and blue parts show the two separate sides of the 2σ region of the star's CCF profile. Another relevant output from our functions is the star's normalised CCF profile with the best-fit rotational profile (bottom left in Fig. 4 from a series of profiles with $v \sin i$ from 1 to 200 km s^{-1}). The legend shows the best fitting profile value and the stretch factor, which is a measure of how much the best-fit $v \sin i$ profile was stretched to achieve the fit. The inset in the

---

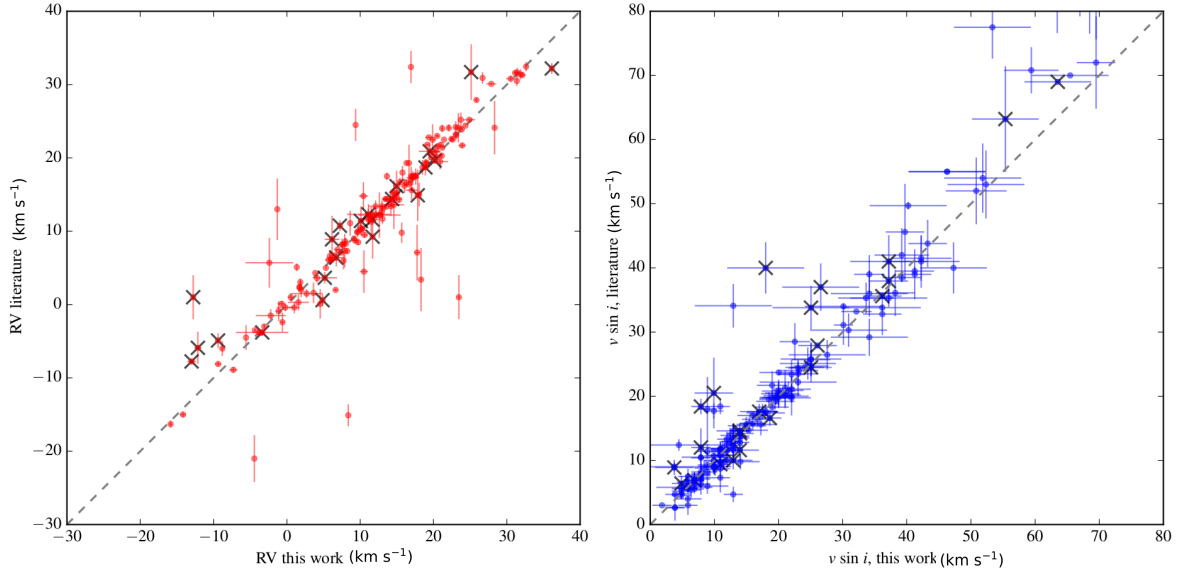[6] Code is available at https://github.com/szunigaf

Fig. 5. *Left panel*: RV values calculated in this work versus the values from the literature. Crosses represent previously identified spectroscopic multiple systems. The 1:1 relation is shown by the dashed line. *Right panel*: same as upper panel, but for $v \sin i$ values.

upper right shows an area around the minimum of the residuals from different $v \sin i$ profile fitting, highlighting in this case that $7 \, \mathrm{km \, s^{-1}}$ is clearly the best fit. We note that these $v \sin i$ values are "raw", see Appendix B for details on calibration. The three metrics of the bisector are also given by our functions (see bottom right panel in Fig. 4); namely the BIS ($\bar{v}_t - \bar{v}_b$), the slope (b_b), and the curvature (c_b) which help to quantitatively characterise the properties of the bisector.

We visually inspected each of the CCF outputs and removed any observations where the CCF calculation had clearly failed (or a different mask had to be used), mostly due to low S/N. This left 1375 CCFs for further analysis. Several broadening mechanisms can contribute to the width of the CCF – these can either be inherent to the star (surface gravity, effective temperature, rotation, turbulence) or arise from the instrument used to obtain the observations. Therefore to accurately measure rotational velocities we have to account for non-rotational broadening mechanisms, both physical and instrumental. The details for our calibration approach can be found in Appendix B.5.

With our calibrated $v \sin i$ values and barycentric RVs, we were able to look at the overall properties of our targets by combining individual observations. We were also able to identify any clear double-lined spectroscopic binaries from their double-peaked CCF profiles (see Appendix A).

For each object, we compared the median RVs and $v \sin i$ from our database with previously published values (see Table 1 for references) to ensure there was no significant offset. Figure 5 shows the results of this comparison. The error bars for each quantity represent the standard deviation from multiple observations.

Black crosses represent objects previously identified as multiple systems, that is, those not likely to follow the 1:1 relation. We also note that for $v \sin i \gtrsim 50 \, \mathrm{km \, s^{-1}}$, the broader CCF profile translates into a larger uncertainty on the estimate of this quantity (see Appendix B). With all of this taken into account, the 1:1 relation describes adequately the comparison of both sets of values for objects considered as a single stars, demonstrating that our new functions calculating CCF properties are working correctly.

6. Using multiple measurements to identify single-lined spectroscopic binaries

Most previous studies identifying SB1 solely rely on the analysis of multi-epoch RV values. However, in this work, we use the high-order CCF features, if possible, when investigating any potential RV variation to better conclude on the true nature of the object. We made an initial list of systems to be further investigated by looking at both RV and $v \sin i$ variation as a function of $v \sin i$.

6.1. Distinguishing RV variation as a function of rotation

Typically, the variation in RV (σ_{RV}) is used to flag potential SB1. However, this apparent variation can also be caused by mechanisms unrelated to multiplicity. Elliott et al. (2014) used a single value (global $\sigma_{\mathrm{RV}} = 2.7 \, \mathrm{km \, s^{-1}}$) to flag potential SB1, irrespective of their $v \sin i$ values. However, in this work we show that σ_{RV} is a function of $v \sin i$, that is, the apparent radial velocity variation is intrinsically related to the target's $v \sin i$. This was also demonstrated in Bailey et al. (2012) using near-infrared radial velocities. The relationship can be explained by the peak of the CCF being less well-defined the broader the profile is. We can exploit this relationship to revisit the spectroscopic multiplicity of stars in our sample.

Figure 6 shows σ_{RV} versus $v \sin i$ for stars in our sample that are not double- or triple-lined spectroscopic binaries, and that have observations for at least two different epochs. The left panel shows the estimates from this work while the right panel presents our values together with those compiled from literature and *Gaia* DR2. For the sake of homogeneity, to be considered, the literature data also has to fulfil the criteria of having an uncertainty on RV and $v \sin i$ lower than 3 and $5 \, \mathrm{km \, s^{-1}}$, respectively (Sect. 2).

Considering only our measurements, we note that the dispersion in RV is relatively low for slow rotators. For example, 3σ variation of 0.7 and $1.1 \, \mathrm{km \, s^{-1}}$ for $v \sin i$ of ≈ 5 and $10 \, \mathrm{km \, s^{-1}}$, respectively (shown by the solid red line in Fig. 6). Only at $v \sin i \approx 40 \, \mathrm{km \, s^{-1}}$ more than $3 \, \mathrm{km \, s^{-1}}$ RV variations are observed. When measurements from the literature are
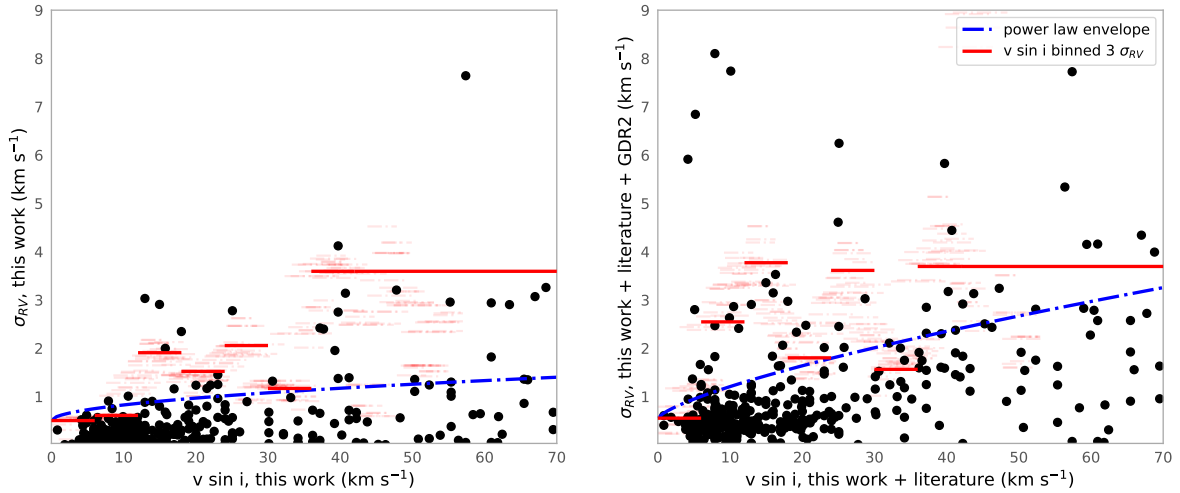
Fig. 6. *Left panel*: standard deviation in RV as a function of $v \sin i$ for measurements calculated in this work. The 3σ value from binning in $6\,\mathrm{km\,s^{-1}}$ bins are represented by the red solid lines. The power-law envelope is represented by dash-dotted blue line. *Right panel*: same as left panel, but including values from the literature and *Gaia* DR2 for the standard deviation estimates.

considered, on average, RV variations increase which is expected from combining observations from different instruments, heterogeneity in the procedure to perform the estimates, and a longer time-span between observations.

As mentioned before, a relationship between $v \sin i$ and σ_{RV} is expected. In order to obtain a general and empirical description this relation, we calculated the 3σ interval for σ_{RV} using an array of binned $v \sin i$ values. We ran a Monte Carlo simulation using the 3σ statistics for different bin size and phase (the starting point of the binning). The bin size range was between 3 and $7\,\mathrm{km\,s^{-1}}$. This range was estimated from the three most commonly used bin-size estimation method: Freedman & Diaconis (1981), Scott (1979) and Sturges (1926). The selected initial phase range covers from 0 to $4\,\mathrm{km\,s^{-1}}$. This exercise allowed us to address the dispersion in the results that can be explained solely in therms of the choice of phase and bin size. Each realisation is represented by a light red line in Fig. 6. It is out of the scope of this work to characterise, in detail, the underlying physical structure between the σ_{RV} values as a function of $v \sin i$. The only purpose of the simple analysis presented here is to have a first order estimate of the effect of the rotation velocity in the RV determination and, consequently, in its variation. The final adopted thresholds to be used as "caution" flags when assessing multiplicity are those resulting from a $6\,\mathrm{km\,s^{-1}}$ step between 0 and $42\,\mathrm{km\,s^{-1}}$ (solid red line, Fig. 6). This bin size was selected by taking in consideration the better compromise between sampling and the minimum number of points in each bin. Beyond $43\,\mathrm{km\,s^{-1}}$ on $v \sin i$, the number of points in each bin is $\lesssim 10$ and, therefore, the statistics become less reliable. However, we can assume that a very rough positive correlation is maintained or, at the very least, that it does not invert, that is, the higher the $v \sin i$, the larger the RV variation is.

As an alternative method to identify SB candidates, we fit a power-law of the form $\sigma_{\mathrm{RV}} = m \, (v \sin i)^b$ and then we scale it up to keep a conservative envelope that leave about 85% of the points below it. The fit is obtained using a Huber loss function (Huber 1964), which is more robust to outliers than squared loss function (Ivezić et al. 2014) and is shown as a dashed-dotted blue line in Fig. 6. We identified SB candidates using both selection criteria and further investigated the nature of any targets with RV

variation lying above either of those thresholds. We investigated the true SB nature of any targets with RV variations above those thresholds (see Table 3 and Appendix A).

6.2. Distinguishing fast rotators from blended binaries

Large projected rotational velocity values could not only result from a single fast rotator, but also from a blended profile of two slower rotators. If the latter is the case, one would expect $v \sin i$ values varying in time depending on the system's phase at the time of the observations. To investigate any potential systems of this kind, similarly to Fig. 6, we looked at the typical variations in $v \sin i$ as a function of median $v \sin i$. These results are shown in Fig. 7. We note that as our $v \sin i$ values are calculated from a grid of rotational profiles with $1\,\mathrm{km\,s^{-1}}$ step, our study is not sensitive to smaller variations and, therefore, many objects appear to be constant. Following a similar approach to the one of the previous subsection, we calculated an upper envelopes to the variations in $v \sin i$ and flagged systems above those levels for further inspection.

6.3. Using the BIS versus RV relation

Another way to validate whether a RV variation is induced by a bound companion is to include the BIS as an additional source of information. Lagrange et al. (2013) used this technique searching for giant planets in a sample of 26 stars, some of which are in the young associations studied here. Significant anti-correlation between the BIS and RV suggests that the RV jitter is most likely due to stellar activity (Desort et al. 2007). This technique relies on a large number of measurements per target and therefore in this work we are limited to a small number of stars in our sample. Therefore, in our case, this technique allowed us to rule out a few potential SBs rather than to identify new systems. The BIS and RV values are listed in Table G.1.

6.4. Spectroscopic binaries from the literature

We searched the literature to identify formerly flagged SBs from our sample to assess the robustness of our method. For all previously identified spectroscopic binaries, we recover a very large
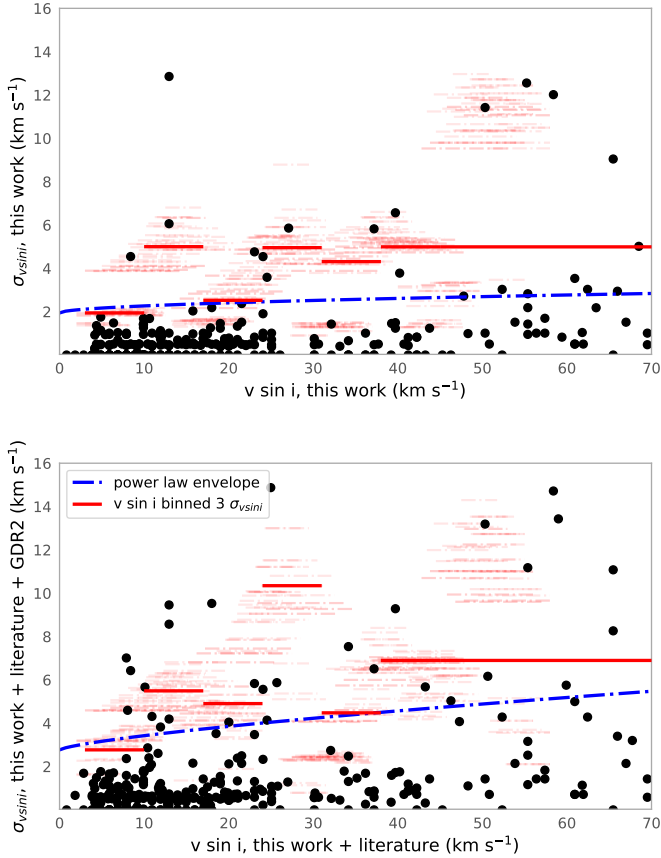
Fig. 7. *Top panel*: $v \sin i$ versus the standard deviation in $v \sin i$ for measurements calculated in this work. The 3σ values, from 3 to $45 \, \mathrm{km \, s^{-1}}$ binned in $7 \, \mathrm{km \, s^{-1}}$ bins, are shown by red solid lines. The power-law envelope is represented by dash-dotted blue line. *Bottom panel*: same as upper panel, however, including values from the literature.

fraction of them ($84\%^{+11}_{-8}$). Most of the non-recovered SBs correspond to objects or systems with very few observations in our local database, but for a few of the objects, our analysis contradicts the "SB flag" found in the literature (see Appendix A for comments on the individual sources).

6.5. Close visual binaries from the literature

Some multiple systems have the right configuration and are located at the right distance for them to be resolvable with direct imaging techniques (with adaptive optics, AO hereafter) and, in addition, display RV variations of the primary. A good example of such system is V343 Nor (Nielsen et al. 2016). Looking for similar cases, we compiled a list of targets from the literature that have AO-discovered known companions (typically, with estimated periods of ≈ 1000 days, Table 2).

Unfortunately, within this AO sample of four close visual binaries, none of them had sufficient time coverage in our database of high-resolution spectra to achieve the sensitivity needed to detect any companion-induced RV changes. However, the orbits of all four systems have been determined in previous works, as noted in Table 2.

6.6. Detection of SBs candidates

The final list of SB candidates identified in this work is presented in Table 3. In a few cases, our analysis contradicts previous

Table 2. Kinematic properties of previously identified close visual binaries within our sample.

ID	σ_{RV} $(\mathrm{km \, s^{-1}})$	$v \sin i$ $(\mathrm{km \, s^{-1}})$	Time span (day)	Num. obs	P (year)	Ref.
TWA 22	0.19	9.9	64	3	5.15	a
HD 98800	0.07	<5	4	2	0.86	b, g
HD 16760	…	<5	…	1	1.27	c, d
HD 36705	…	≈ 75	…	1	11.74	e, f

References. a: Bonnefoy et al. (2009), b: Malkov et al. (2012), c: Bouchy et al. (2009), d: Sato et al. (2009), e: Close et al. (2005), f: Nielsen et al. (2005), g: Torres et al. (1995).

claims of multiplicity from the literature, while in some other cases, we do not recover the SB nature of some candidates, which we attribute to the sampling of the data available to us (see details on Appendix A).

Out of the 381 objects from the compilation of our work, the literature (Table 1) and *Gaia* DR2, we identified 68 SB candidates. For each candidate, we compiled all the information available regarding RV and $v \sin i$ both from our work and the literature. We used those values to establish a final classification regarding their multiplicity. The conclusion (*Conc.*) column of Table 3 presents the summary of this analysis, where the values "Y", "N", or "?" correspond to "multiple system", "not a multiple system according to the data available", or "inconclusive".

While specific comments for particularly interesting or challenging candidates can be found in Appendix A, there were a number of cases where the variable flag of $v \sin i$ turned out to be a misleading diagnostic. In these cases, a closer inspection of the CCF profiles revealed that the variability was not real and, rather, simply induced by a poor fitting of the rotational profile. In such cases, it is still possible that the candidate is an unresolved SB, but since we do not have sufficient evidence to support that conclusion, we flagged those candidates as inconclusive.

7. Accounting for observation sensitivity

As we have seen through this work, tight binaries can be detected in spectroscopic data via identification of double (or multiple) lines, variable RVs (or, unrelated to this work, even unexpected mixes of spectroscopic features). However, our ability to identify these features (multiple lines and variations in RV), can be severely biased by factors such as: the observations strategy (time span T and number of measurements N_{obs}) and the inherent sensitivity of the spectrographs employed for the observations. These factors have been thoroughly studied and modelled by Tokovinin (2014a). The steps incorporated in our analysis to translate this knowledge into detection probability maps were the following:

Firstly, we created a set of 10 000 simulated binaries from the following distributions: Period (p) log-normal ($\mu = 5.03$, $\sigma = 2.28$ log(day), Raghavan et al. 2010). Mass ratio (q) uniform (for system between 0.01-1.0 $M_\odot$; Raghavan et al. 2010; Kraus et al. 2011; Elliott et al. 2015). Eccentricity (e), two-part: $p \leq 12$ days, $e = 0$; $p > 12$ days, uniform (for $0 \leq e \leq 0.6$). Initial phase (ϕ_0), longitude of ascending mode (ω) and inclination (i) uniform (for $0 \leq \phi_0 \leq 1$, $0 \leq \omega \leq 2\pi$, and $0 \leq i \leq \pi$, respectively).

Table 3. Properties of targets flagged as potential SB1 systems in the analysis presented in this work.

ID	Values calculated in this work				Values calculated in this work + literature				# obs	Flag	Conc.
	RV_{median}	σ_{RV}	$v \sin i_{median}$	$\sigma_{v \sin i}$	RV_{median}	σ_{RV}	$v \sin i_{median}$	$\sigma_{v \sin i}$			
Potential SB1 systems from variable RV and/or $v \sin i$ values											
CD-46 644	23.70	0.03	34.16	0.0	24.22	0.96	34.16	7.54	2 (4)		N
HD 17332 A	4.62	0.75	8.41	4.55	4.20	0.66	8.41	4.55	2 (4)		?
CD-56 1032A	31.87	4.12	39.72	6.56	31.87	5.83	39.72	9.28	2 (2)		Y
CPD-19 878	25.59	1.32	30.63	0.51	25.59	1.32	30.63	0.51	4 (4)		?
TYC 7627-2190-1	21.94	3.03	12.95	12.85	21.94	3.71	24.98	14.88	3 (4)		Y
V*PXVir	−12.99	0.52	4.17	0.31	−12.39	5.81	4.16	0.35	4 (8)	SB1	Y
HD 159911	21.77	0.63	58.4	12.02	21.77	0.63	58.4	12.02	3 (3)		Y
CD-43 3604	17.5	2.35	18.0	2.19	17.43	2.66	18.0	9.52	4 (5)		Y
V* V379 Vel	14.645	0.045	7.9	1.5	14.6	1.49	7.9	1.5	2 (3)		?
TYC 8594-58-1	11.03	0.650	12.95	0.0	11.03	0.75	12.95	9.45	4 (5)		N
2MASS J12203437-7539286	4.86	0.02	7.9	1.5	4.86	2.47	7.90	2.37	2 (3)		Y
HD 129496	−6.07	3.07	66.99	1.51	−6.07	3.07	66.99	1.51	2 (2)		N
V*AFLep	20.89	1.11	50.32	11.42	21.39	1.25	50.32	11.42	4 (5)		N
HD 139084	5.17	1.99	15.77	0.56	5.10	1.76	15.88	0.55	9 (11)	SB1	Y
HD 139084 B	4.55	0.01	15.98	1.50	2.32	3.14	15.98	1.5	1 (2)		N
HD 164249 A	−0.14	1.17	21.54	2.37	−0.09	1.06	21.03	2.25	8 (11)		N
HD 164249 B	−0.6	0.28	12.95	6.06	−0.88	0.88	12.95	6.06	2 (3)		N
CD-31 16041	−8.81	0.20	40.22	3.78	−8.73	1.25	43.25	4.92	3 (4)		N
V*PZTel	−2.99	2.96	55.23	12.55	−3.54	2.71	58.99	12.81	10 (12)		N
HD 199143	−22.73	...	58.40	...	−13.62	12.89	92.95	48.86	1 (2)		N
*cEri	18.48	7.64	57.39	1.69	18.43	7.23	57.39	1.69	7 (8)		N
GJ 3305	23.91	0.49	5.88	0.48	20.95	1.57	5.88	0.48	3 (9)		Y
HD 22213	11.27	3.14	40.73	0.51	11.27	3.14	40.73	0.51	2 (2)		Y
HD 21997	17.17	0.86	65.47	9.05	17.24	0.91	65.47	9.05	3 (4)		N
V*AGLep	25.31	0.57	23.050	4.76	25.31	0.57	23.050	4.76	4 (5)		?
CD-44 753	13.16	0.91	7.9	0.95	13.78	1.37	7.0	0.95	3 (6)		N
HD 104467	11.16	2.78	25.07	2.25	11.4	2.31	25.07	2.25	6 (8)		Y
2MASS J12020369-7853012	11.17	2.91	14.97	0.71	11.17	2.91	14.97	0.71	4 (4)	SB1	Y
BD-184452A	...	...	...	...	−19.31	2.01	8.05	4.59	0 (2)		?
GSC 08057-00342	...	...	...	...	13.5	5.59	5.2	...	0 (3)	SB1	Y
2MASS J04470041-513440	...	...	...	...	17.92	1.98	5.1	...	0 (2)		N
UCAC3 33-129092	...	...	...	...	7.07	2.86	10.5	...	0 (2)		N
UCAC4 110-129613	...	...	...	...	3.58	6.24	25.1	...	0 (2)		N
CD-53 544	12.62	2.90	63.45	2.18	12.56	2.55	65.47	8.26	3 (5)		N
TYC8098-414-1	...	...	...	...	19.53	8.72	11.75	9.40	0 (6)		?
HD 207575	1.42	2.42	37.19	5.82	1.5	2.14	37.19	5.82	5 (7)		?
HD 207964	23.46	0.2	53.86	1.52	23.26	12.65	53.86	1.52	2 (3)		N
TYC 9344-293-1	6.16	1.01	55.37	1.43	6.95	1.57	55.35	10.0	3 (6)		N
UCAC3 92-4597	...	...	...	...	−5.2	9.81	4.7	...	0 (3)	SB	Y
HD 3221	−2.39	3.26	68.5	5.01	−2.39	3.26	68.5	5.01	3 (3)		N
UCAC3 70-2386	...	...	...	...	5.65	2.33	19.2	...	0 (2)	SB	Y
V* CE Ant	11.7	0.06	4.87	1.75	12.4	0.32	4.87	1.76	4 (17)		N
TWA23	10.82	0.04	9.92	3.0	7.71	2.61	9.92	3.0	2 (16)	SB	Y
UCAC2 1331888	−1.66	0.56	25.07	1.0	−2.22	2.01	25.80	1.09	2 (3)		N
HD 48189	36.14	0.01	16.99	1.5	33.40	2.06	17.29	0.43	2 (3)		N
CD-30 3394	12.71	2.39	37.69	0.50	14.99	2.84	37.19	0.87	4 (5)		?
CD-30 3394B	13.94	3.21	47.79	2.71	15.09	3.24	47.29	4.07	4 (5)		?
CD-52 9381	−13.85	2.74	39.71	1.23	−13.85	2.74	39.71	1.23	4 (4)		N
GSC 08350-01924	1.57	1.45	23.05	3.0	0.21	1.46	23.05	3.0	2 (4)		N
V*AFHor	12.91	0.06	7.90	1.5	12.70	1.13	7.90	1.58	2 (6)		N
RX J12204-7407	14.60	1.37	39.72	1.5	14.60	1.58	39.71	1.72	4 (4)		N
[FLG2003] eps Cha 7	13.64	1.24	23.05	0.47	13.64	1.24	23.05	0.47	3 (3)		N
HD 17250	10.51	0.54	42.24	0.82	9.73	2.92	42.24	1.01	3 (5)	SB	Y
HD 191089	−11.69	0.47	43.75	1.23	−11.18	3.13	43.75	1.42	4 (7)		?
V* AO Men	16.02	0.22	16.69	0.44	16.02	1.63	16.69	0.44	8 (10)		N
HD 984	−2.21	1.95	39.26	1.45	−2.21	2.30	39.26	1.59	6 (8)		N
HD 37484	21.19	0.13	52.34	1.5	21.32	2.80	52.34	1.5	2 (3)		N
2MASS J01505688-5844032	...	...	...	...	9.95	1.62	10.10	...	0 (2)		N
UCAC4 137-000439	...	...	...	...	7.69	2.41	11.20	...	0 (2)		?
2MASS J12560830-6926539	...	...	...	...	11.31	3.53	16.30	...	0 (2)		Y
BD-20 1111	19.26	0.72	24.06	4.54	18.68	1.00	24.06	5.56	3 (4)		?
Smethells 165	5.98	0.72	20.02	0.47	6.04	0.69	20.02	4.04	3 (6)		?

Notes. Standard deviation are calculated for targets with two or more epochs. Targets previously flagged but not recovered in this work are available in Appendix A. The new and recovered SB2 and SB3 targets are available in Appendix A and Table G.4.

From our simulations and using Eqs. (5)–(7) from Tokovinin (2014a), we calculated a detection probability map for each object characterised by its three detection parameters (N_{obs}, T and σ_{RV}). In the case of single epoch data, we assumed the same artificial parameters used by Tokovinin (2014a) (i.e. $T = 100$ days, $N_{obs} = 3$, and $\sigma_{RV} = 2$ km s^{-1}), since we are still sensitive to double- and triple-lined multiple systems.

The detection map of each object was calculated on the same mass ratio versus period grid. This "common-grid" approach makes it easy to average those maps for objects belonging to the same moving group, yielding an average sensitivity map per association in our sample (see Fig. 8).

These "association-averaged" probability maps were used to correct our SB fractions from biases induced by the observation strategy and precision. The correction was calculated by taking the mean value in the parameter space $0.1 \leq q \leq 1$ and $p \leq 10^{3.2}$ days. We excluded mass ratios smaller than 0.1 as very few targets have any meaningful probability of detection in this parameter space (Fig. 8, color-scale from red, 100%, to white, 0%).

We note that these corrections are applied across the entire parameter space and do not have assumptions regarding the underlining mass ratio or period distributions (as we have extremely limited information on both).

8. Updated census of spectroscopic binaries

Building from the previous sections, in Fig. 9, we present the SB fraction obtained for each associations as a function of the median $v \sin i$ of its members. In that figure we present both fractions: the original one that disregards the effects discussed in Sect. 7, and the "corrected" one (blue and red symbols, respectively). The uncertainties on the derived fractions are calculated from binomial statistics (Burgasser et al. 2003).

As mentioned earlier in this paper, it is extremely difficult to fully account for the effect of $v \sin i$ on the sensitivity in order to identify SBs. Since fast rotators may bias the resulting SB fractions, we opted to look for any relationship between the obtained SB and the median $v \sin i$ of the members of each association. No apparent correlation was found between those two quantities, and the distribution of $v \sin i$ values for each association are plotted in Fig. 10.

One striking result from our study is that the SB fraction obtained for the TW Hya association seems to contradict the results from Elliott et al. (2014). This difference is driven by the discovery of three newly identified SBs in this work, which was possible because of an increase of 30% in the amount of data available for this association since Elliott et al. (2014). To test this result against membership criteria, we compared the fraction estimated using the census obtained from the BANYAN Σ tool with that of the convergence method and found both figures to be fully compatible (see Fig. 11).

Interestingly, the three highest SB fractions are found for the three youngest associations (ϵ Cha 18^{+15}_{-11}%, TW Hya 22^{+16}_{-14}% and β Pictoris moving group 24^{+9}_{-8}% prior sensitivity correction, and 22^{+15}_{-11}%, 32^{+16}_{-12}%, and 33^{+9}_{-8}%, respectively, when the corrections of Sect. 7 are applied). This is unlikely to result from a lack of sensitivity due to large rotational broadening, as the median $v \sin i$ values are relatively low and similar (once the low-number statistics are taken into account) for the three associations (see Fig. 10). Furthermore, as shown in Fig. 11, the higher SB fraction of these associations seems to be insensitive to the membership criteria used, appearing also when the BANYAN Σ cen-
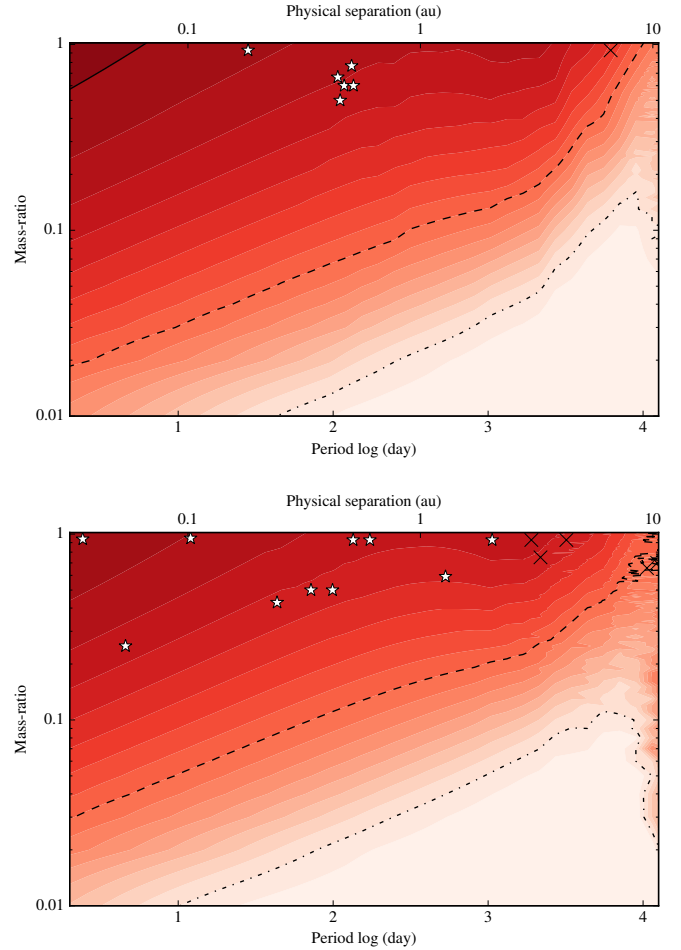

Fig. 8. *Upper panel*: average detection probabilities for THA association (contours from red, 100%, to white, 0%), detected spectroscopic companions (white stars) and visual binaries (black crosses) in the physical separation versus mass ratio. The solid, dashed and dash-dotted lines encompass areas with detection probabilities ≥90%, 50%, and 10 %, respectively. *Bottom panel*: same as upper panel, but for BPC association.

sus is employed. On the other hand, the average SB fraction for the five older associations are ≲10% (with the possible "intermediate" case of THA). It must be noted that the confidence interval for this "dichotomy" is only 1–2σ given the large associated uncertainties.

9. Discussion

The results presented in Sect. 8 suggest a counter-intuitive path of evolution for SBs. In this section, we compare our results to the literature, discuss whether these results are, in fact, an artefact produced by our methodology or a physical result; and, in the latter case, whether we are really witnessing early SB evolution or the effect of other environmental factors.

9.1. Comparison with previous results on low density environments

Figure 11 shows SB fractions (≈10%) consistent with the field population (≈10%, Raghavan et al. 2010; Tokovinin 2014b), the young clusters Tau-Aur, and Cha I (≈7%, Nguyen et al. 2012), and our previous results from Elliott et al. (2014) for
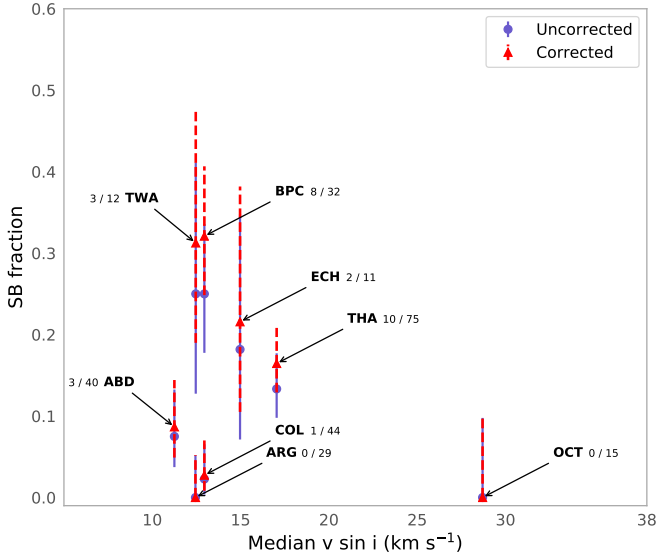
Fig. 9. SB fraction as a function of median $v \sin i$. The uncorrected SB fractions are shown in purple and in text next to the name of each association. The corrected SB fractions are shown in red. The primary mass range is $0.6 \leq M \leq 1.5\,M_\odot$.
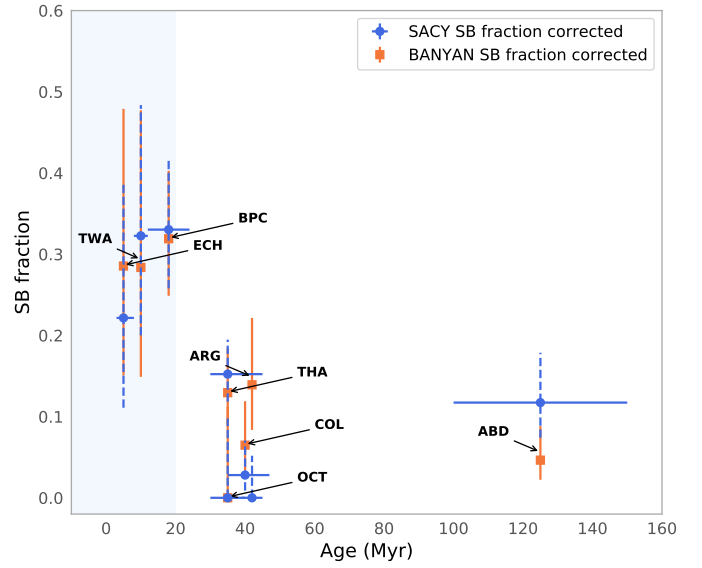

Fig. 11. Corrected SB fraction as a function of age (Myr) for membership estimation from our convergence method (blue dots, Torres et al. 2006, 2008) and BANYAN Σ (orange dots, Gagné et al. 2018). The shaded area highlights the ≤ 20 Myr zone of the figure. The primary mass range is $0.6 \leq M \leq 1.5\,M_\odot$.
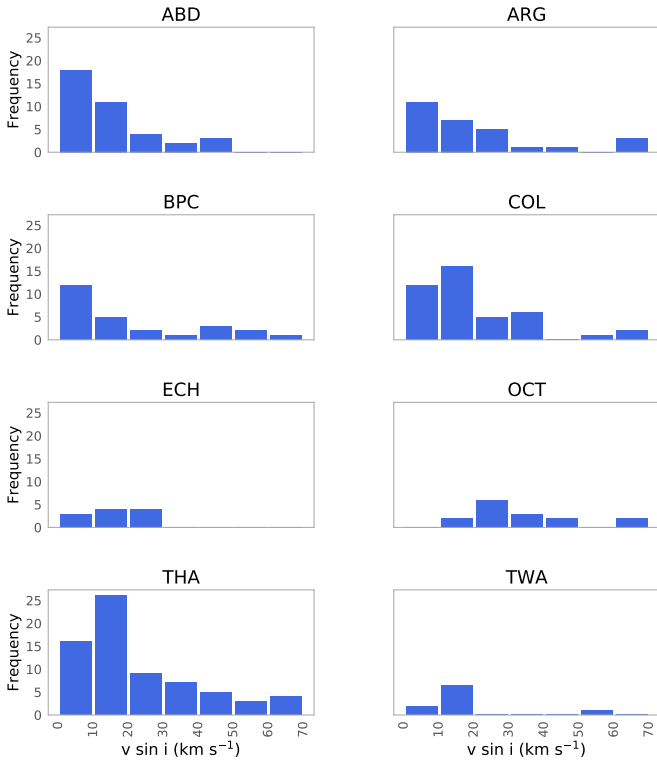
Fig. 10. $v \sin i$ histogram for each young association from this work with a primary mass range of $0.6 \leq M \leq 1.5\,M_\odot$.

the five older associations ($\gtrsim 20$ Myr) across the mass range of $\sim 0.2-2.0\,M_\odot$. On the other hand, the observed SB fractions for the three youngest associations seem to be larger than those reported for the previously mentioned young regions of Tau-Aur (1 Myr) and Cha I (2 Myr). The estimated distances to these young regions are ~ 140 pc and ~ 160 pc, respectively (Nguyen et al. 2012); therefore, we argue that, given the overall closer distance of our targets, the difference should not

arise from a lack of sensitivity or a completeness bias in the SACY sample (see Sect. 5 from Nguyen et al. 2012).

Nevertheless, the relative paucity of SBs in Tau-Aur and Cha I could be explained by the sample used by Nguyen et al. (2012), which is concentrated on the higher stellar density regions of the clouds. For instance, Guieu et al. (2006) revisited the previously claimed brown dwarf deficit in the same Tau-Aur region, performing a larger scale optical survey including the surroundings of the clouds as well as their densest parts. The authors concluded that the possible deficit was in fact an artefact from target selection rather than a real difference. Interestingly, Viana Almeida et al. (2012) derived an SB fraction of $\approx 42\%$ for the Rho Ophiuchus star forming region ($\sim 0.1-1$ Myr) from targets with mass range of $\sim 0.18-1.4\,M_\odot$ (Natta et al. 2006) and a binary fraction of $\approx 71\%$ combining data from different works. These results are more consistent with the SB fraction of our youngest associations and are aligned with the notion that multiplicity is very high at young ages (younger than ~ 1 Myr). Although the statistical significance in the difference on SB fraction in Fig. 11 is weak, at the level of $1-2\sigma$, it is hard to reconcile with the general picture of SB fraction remaining unchanged after ~ 1 Myr. Therefore, it deserves independent confirmation and further characterisation.

9.2. The impact of the sensitivity correction

In Sect. 7, we created sensitivity maps from 10 000 simulated binaries to estimate how many binary systems would have been missed because of our observing strategy. The simulated binaries were drawn according to certain priors on the mass ratio, period, and orbital parameters, but those parental distributions were originally estimated from field star surveys (Raghavan et al. 2010; Tokovinin 2014a). Those priors may not be representative of the underlying population of binary stars in young associations ($\lesssim 100$ Myr). This may have consequences on the sensitivity corrections we obtained which may lead to an artificially large value for the corrected SB fraction.

The prior on the period distribution is the most critical one, as it has the most significant effect on the detection probability (shorter periods are easier to detect using spectroscopic observations). Taking this into consideration, we created new sensitivity maps using a log-normal period distribution ($\mu = 5.3$, $\sigma = 2.28 \log(\text{day})$, from Tobin et al. 2016), representative of Class 0/I systems ($\lesssim 1$ Myr). With this period distribution, we obtain an increase of ~2% on the correction factor. This slight increase is not sufficient to explain the difference of $\gtrsim 10-20\%$ between the three younger associations with respect to the older ones in our sample. We further tested the impact of the period distribution on the correction factor by taking an even more extreme case. We used a distribution centred at the smallest separation that a primordial binary system could have (≈ 10 au from disc fragmentation; Vaytet et al. 2012). Even in that almost unrealistic scenario, we did not reach a change of sensitivity sufficient to justify the differences of SB fractions between the young and old associations in our sample. The analysis presented here suggests that the differences in SB fractions are not artificially created by our sensitivity correction approach.

9.3. Relation with higher-order multiplicity

From the SBs identified in this work, $\sim 77^{+8}_{-7}\%$ are also part of higher-order multiple systems (Elliott et al. 2016; Elliott & Bayo 2016). This shows a preference for SBs to be found in triple or higher-order systems, similar to the 63% reported in Tokovinin et al. (2006) for field stars.

There is observational evidence that suggests an overall decrease of binary fraction from pre-MS ages to field ages (Ghez et al. 1997; Kouwenhoven et al. 2007; Raghavan et al. 2010). Elliott & Bayo (2016) suggested that dynamical interactions of triple systems (as proposed by Sterzik & Tokovinin 2002; Reipurth & Mikkola 2012) could explain the population from close (0.1 au) to very wide (10 kau) tertiary components where the majority of the wide companions are in the process of being disrupted on timescales of $10-100$ Myr. The results of Raghavan et al. (2010) also suggest that systems with long periods, or those with more than two components, tend to lose companions with age due to dynamical evolution. However, such mechanisms, which would explain the disruption of wide companions but would not necessary explain the SB fraction in this sample. In fact, Tokovinin et al. (2006) suggested that the overall SB fraction seems to remain unchanged after ~1 Myr.

Supporting the dissolution scenario, proposed by Sterzik & Tokovinin (2002), Reipurth & Mikkola (2012), $\sim 92^{+13}_{-6}\%$ of SBs in the three youngest associations studied here are part of a triple or high-order multiple system that stand in contrast with the $\sim 67^{+12}_{-11}\%$ for the five older associations.

9.4. SB fraction evolution with age

Our results hint that the youngest associations ($\lesssim 20$ Myr) may have a larger SB fraction, even though it remains tentative at the moment. This result suggests a possible decrease of the SB fraction from ~5 to ~100 Myr. A similar result was obtained for the IN-SYNC (INfrared Spectroscopy of Young Nebulous Clusters) sample from high resolution H-band spectra observations of low-mass stars in Orion A, NGC 2264, NGC 1333, IC 348, and the Pleiades (Jaehnig et al. 2017), where the SB fraction of the five pre-MS clusters ($\approx 1-10$ Myr) was $\approx 20\%-30\%$ in contrast with $\approx 5\%-10\%$ found for the Pleiades (≈ 100 Myr). Jaehnig et al. (2017) claim that the time sampling of their observations make it more sensitive to the critical 10^2-10^4 day period

range where binary systems are wide enough to be disrupted by dynamical interaction over ~100 Myr timescale in dense environments. However, this scenario is proposed for clusters with typical densities of $\approx 30\,M_\odot\,\text{pc}^{-3}$ (at the core radius, Piskunov et al. 2007) and may not be compatible with the typical densities of ≈ 0.01 stars pc^{-3} for loose associations such as those in the SACY sample (Moraux 2016).

9.5. Role of the environment

The tentative variations in SB fraction could be related to differences in the primordial multiplicity depending on the formation history and environment of the associations. In Fig. 12, we show the sub-spaces of the UVWXYZ-space for all the associations studied in this paper to search for possible signs of clustering in both velocity and spatial coordinates. Given the proximity of the SACY associations no clear separated groups of points appear for the spatial coordinates (Torres et al. 2006). However, it is more informative to plot the galactic proper motion to trace a possible common origin (UVW: positive toward the Galactic center, Galactic rotation, and North Galactic Pole respectively). Qualitatively, we identify possible clustering of points in the UVW sub-spaces (first row of Fig. 12) for the three youngest associations (blue coloured symbols) that may suggest possible common birth place in the Galactic bars for these associations compared to the older ones.

Furthermore, previous studies have found evidence that the three associations, β Pictoris, TW Hya, and ϵ Cha possibly formed in or near the Sco-Cen giant molecular cloud $5-15$ Myr ago (Mamajek et al. 2001; Torres et al. 2008). Then the difference in the SB fraction presented in this work could arise from different primordial multiplicity instead of being caused by their dynamical evolution. Standing in support of the latter argument, the overall binary fraction in Sco-Cen is $\approx 93\%$ among solar-type stars and $\approx 75\%$ among low-mass star (Kouwenhoven 2006). These figures are higher than the overall binary fraction for solar-type and low-mass stars in Tau-Aur reported by Kraus et al. (2011, $\sim 66-75\%$, with slightly different binary parameter space explored). In addition, Clark Cunningham et al. (2020) recently claimed that the ABD association may be kinematically linked to a newly discovered "stellar string" Theia 301. Kounkel & Covey (2019) argue that although they recover Sco-Cen in their kinematic clustering searches, this association is different than the "typical strings" such as Theia 301. To summarise, there are hints supporting non-universal multiplicity, however, our current data-set does not allow us to confirm different environmental star-formation histories among the SACY associations.

10. Summary and conclusions

In this work, we present an update for the SB census for the associations within SACY. Our study is based on new observational data (as well as literature and archival data), as well as new criteria to identify these tight binaries. We have estimated radial and rotational velocity for 1375 spectra using CCFs and compiled ~400 RV measurements from the literature (including *Gaia* DR2, Gaia Collaboration 2018). Our RVs and $v \sin i$ estimates are in good agreement with previously published values, following a 1:1 relation with values from the literature (for targets that are not identified as a multiple systems), demonstrating that our CCF analysis is robust. Further robustness is provided by the fact that we have recovered the $84^{+11}_{-8}\%$ of previously known multiple systems.
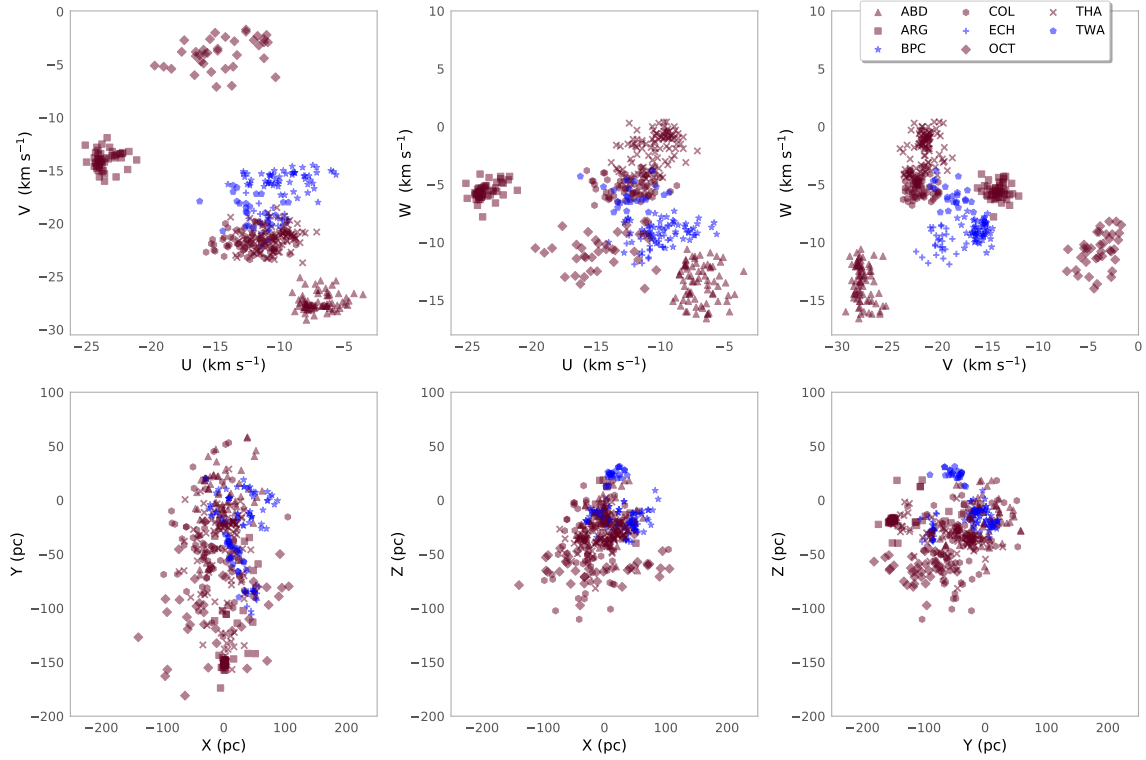
Fig. 12. Combinations of the sub-spaces of the UVWXYZ-space for the young associations in the SACY sample. The blue coloured symbols correspond to the three youngest associations (BPC, ECH and TWA). The full membership study and further analysis will be presented in Torres et al. (in prep.).

Besides RV variations proving to be key in identifying SB candidates, we used high-order cross-correlation functions as a complementary diagnostic tool. These features offer a concrete way to quantify the symmetry, curvature, and quality of the fitting of the CCFs. More epochs do not only allow us to improve the reliability of any RV variation, but it also allows for other statistics to be used when assessing the binary nature of a candidate (see Sect. 6.3, for instance).

We calculated the SB fraction for each SACY association and estimated a correction factor taking into account possible sensitivity issues and biases from the observations (see Sect. 7). The summary of SB candidates can be found in Tables 3 and G.4. The analysis and conclusions reached for each target flagged as a candidate can be found in Appendix A.

We find that the three youngest associations have higher SB fractions overall (ϵ Cha $22^{+15}_{-11}\%$, TW Hya $32^{+16}_{-12}\%$ and β Pictoris moving group $33^{+9}_{-8}\%$ when the corrections of Sect. 7 are applied) compared with the five oldest associations in the SACY sample ($\sim 35-125$ Myr), which are $\sim 10\%$ or lower. This results seems to be independent of the method used for membership assessment (see Fig. 11) and not artificially created by the sensitivity correction approach (see Sect. 9.2). In addition, more than 90% of the SB identified in ϵ Cha, TW Hya and β Pictoris are part of a triple or hierarchical system in contrast with $\approx 70\%$ of the five older associations. While the difference in the SB fraction remains tentative at the moment, we propose two possible explanations: an evolution effect (previously reported in denser environments) and a primordial non-universal multiplicity. With the data currently available, we cannot distinguish between the two possibilities.

References

Aller, A., Lillo-Box, J., Jones, D., Miranda, L. F., & Barceló Forteza, S. 2020, A&A, 635, A128

Astropy Collaboration (Robitaille, T. P., et al.) 2013, A&A, 558, A33

Astropy Collaboration (Price-Whelan, A. M., et al.) 2018, AJ, 156, 123

Bailey, J. I., White, R. J., Blake, C. H., et al. 2012, ApJ, 749, 16

Baraffe, I., Homeier, D., Allard, F., & Chabrier, G. 2015, A&A, 577, A42

Baranne, A., Queloz, D., Mayor, M., et al. 1996, A&AS, 119, 373

Bate, M. R. 2019, MNRAS, 484, 2341

Bate, M. R., Bonnell, I. A., & Bromm, V. 2002, MNRAS, 336, 705

Boisse, I., Eggenberger, A., Santos, N., et al. 2010, A&A, 523, A88

Bonnefoy, M., Chauvin, G., Dumas, C., et al. 2009, A&A, 506, 799

Bonnell, I. A., & Bate, M. R. 1994, MNRAS, 271, 999

Bouchy, F., Hébrard, G., Udry, S., et al. 2009, A&A, 505, 853

Burgasser, A. J., Kirkpatrick, J. D., Reid, I. N., et al. 2003, ApJ, 586, 512

Chauvin, G., Vigan, A., Bonnefoy, M., et al. 2015, A&A, 573, A127

Clark Cunningham, J. M., Felix, D. L., Dixon, D. M., et al. 2020, AJ, accepted, [arXiv:2009.03872]

Close, L., Lenzen, R., Guirado, C., J., , et al. 2005, Nature, 433, 286

Connelley, M. S., Reipurth, B., & Tokunaga, A. T. 2008, AJ, 135, 2526

Cutispoto, G., Pastori, L., Pasquini, L., et al. 2002, A&A, 384, 491

Dall, T. H., Santos, N. C., Arentoft, T., Bedding, T. R., & Kjeldsen, H. 2006, A&A, 454, 341

Dekker, H., D'Odorico, S., Kaufer, A., Delabre, B., & Kotzlowski, H. 2000, in Optical and IR Telescope Instrumentation and Detectors, eds. M. Iye, & A. F. Moorwood, SPIE Conf. Ser., 4008, 534

de la Reza, R., Torres, C. A. O., Quast, G., Castilho, B. V., & Vieira, G. L. 1989, ApJ, 343, L61

Delfosse, X., Forveille, T., Beuzit, J.-L., et al. 1999, A&A, 344, 897

Desidera, S., Covino, E., Messina, S., et al. 2015, A&A, 573, A126

Desort, M., Lagrange, A.-M., Galland, F., Udry, S., & Mayor, M. 2007, A&A, 473, 983

Duchêne, G., Bontemps, S., Bouvier, J., et al. 2007, A&A, 476, 229

Elliott, P., & Bayo, A. 2016, MNRAS, 459, 4499

Elliott, P., Bayo, A., Melo, C. H. F., et al. 2014, A&A, 568, A26

Elliott, P., Huélamo, N., Bouy, H., et al. 2015, A&A, 580, A88

Elliott, P., Bayo, A., Melo, C. H. F., et al. 2016, A&A, 590, A13

Flagg, L., Shkolnik, E. L., Weinberger, A., et al. 2020, ApJ, 896, 153

Freedman, D., & Diaconis, P. 1981, Zeitschrift fur Wahrscheinlichkeitstheorie und Verwandte Gebiete, 57, 453

Gagné, J., Mamajek, E. E., Malo, L., et al. 2018, ApJ, 856, 23

Gaia Collaboration (Brown, A. G. A., et al.) 2018, A&A, 616, A1

Ghez, A. M., McCarthy, D. W., Patience, J. L., & Beck, T. L. 1997, ApJ, 481, 378

Gontcharov, G. A. 2006, Astron. Lett., 32, 759

Grandjean, A., Lagrange, A. M., Keppler, M., et al. 2020, A&A, 633, A44

Gray, D. F. 1976, The Observation and Analysis of Stellar Photospheres (New York: Wiley)

Griffin, R. F. 2010, Observatory, 130, 125

Guieu, S., Dougados, C., Monin, J.-L., Magnier, E., & Martín, E. L. 2006, A&A, 446, 485

Howell, S. B., Sobeck, C., Haas, M., et al. 2014, PASP, 126, 398

Huber, P. J. 1964, Ann. Math. Statist., 35, 73

Ivezić, Ž., Connelly, A. J., Vand erPlas, J. T., & Gray, A. 2014, Statistics, Data Mining, and Machine Learning in Astronomy (Princeton NJ: Princeton University Press)

Jaehnig, K., Bird, J. C., Stassun, K. G., et al. 2017, ApJ, 851, 14

Janson, M., Durkan, S., Hippler, S., et al. 2017, A&A, 599, A70

Johnson-Groh, M., Marois, C., Rosa, R. J. D., et al. 2017, AJ, 153, 190

Kastner, J. H., Zuckerman, B., Weintraub, D. A., & Forveille, T. 1997, Science, 277, 67

Katz, D., Sartoretti, P., Cropper, M., et al. 2018, A&A, 622, A205

Kaufer, A., Stahl, O., Tubbesing, S., et al. 1999, Messenger, 95, 8

Konopacky, Q. M., Ghez, A. M., Duchêne, G., McCabe, C., & Macintosh, B. A. 2007, AJ, 133, 2008

Kounkel, M., & Covey, K. 2019, AJ, 158, 122

Kouwenhoven, M. B. N. 2006, PhD thesis, Anton Pannekoek Institute for Astronomy, Universiteit van Amsterdam, The Netherlands

Kouwenhoven, M. B. N., Brown, A. G. A., Portegies Zwart, S. F., & Kaper, L. 2007, A&A, 474, 77

Kraus, A. L., Ireland, M. J., Martinache, F., & Hillenbrand, L. A. 2011, ApJ, 731, 8

Kraus, A. L., Shkolnik, E. L., Allers, K. N., & Liu, M. C. 2014, AJ, 147, 146

Lagrange, A.-M., Meunier, N., Chauvin, G., et al. 2013, A&A, 559, A83

Lee, J., & Song, I. 2019, MNRAS, 489, 2189

Lopez-Santiago, J., Montes, D., Crespo-Chacon, I., & Fernandez-Figueroa, M. J. 2006, ApJ, 643, 1160

Macintosh, B., Max, C., Zuckerman, B., et al. 2001, Young Stars Near Earth: Progress and Prospects, eds. R. Jayawardhana, & T. Greene, ASP Conf. Ser., 244, 309

Maldonado, J., Martínez-Arnáiz, R. M., Eiroa, C., Montes, D., & Montesinos, B. 2010, A&A, 521, A12

Malkov, O. Y., Tamazian, V. S., Docobo, J. A., & Chulkov, D. A. 2012, A&A, 546, A69

Malo, L., Artigau, É., Doyon, R., et al. 2014, ApJ, 788, 81

Mamajek, E. E., & Feigelson, E. D. 2001, in Young Stars Near Earth: Progress and Prospects, eds. R. Jayawardhana, & T. Greene, ASP Conf. Ser., 244, 104

Mayor, M., Pepe, F., Queloz, D., et al. 2003, Messenger, 114, 20

Melo, C. H. F. 2003, A&A, 410, 269

Melo, C. H. F., Pasquini, L., & De Medeiros, J. R. 2001, A&A, 375, 851

Merle, T., der Swaelmen, M. V., Eck, S. V., et al. 2020, A&A, 635, A155

Mochnacki, S. W., Gladders, M. D., Thomson, J. R., et al. 2002, AJ, 124, 2868

Montes, D., López-Santiago, J., Fernández-Figueroa, M. J., & Gálvez, M. C. 2001, A&A, 379, 976

Moór, A., Szabó, G., Kiss, L., et al. 2013, MNRAS, 435, 1376

Moraux, E. 2016, in EAS Publ. Ser., 80-81, 73

Murphy, S. J., Lawson, W. A., & Bento, J. 2015, MNRAS, 453, 2220

Natta, A., Testi, L., & Randich, S. 2006, A&A, 452, 245

Nguyen, D. C., Brandeker, A., van Kerkwijk, M. H., & Jayawardhana, R. 2012, ApJ, 745, 119

Nielsen, E., Close, L., Guirado, J., et al. 2005, Astron. Nachr., 326, 1033

Nielsen, E. L., Rosa, R. J. D., Wang, J., et al. 2016, AJ, 152, 175

Nordstrom, B., Olsen, E. H., Andersen, J., Mayor, M., & Pont, F. 1996, in The History of the Milky Way and Its Satellite System, eds. A. Burkert, D. H. Hartmann, & S. A. Majewski, ASP Conf. Ser., 112, 145

Ochsenbein, F., Bauer, P., & Marcout, J. 2000, ApJS, 143, 23

Piskunov, A. E., Schilbach, E., Kharchenko, N. V., Röser, S., & Scholz, R. D. 2007, A&A, 468, 151

Povich, M. S., Giampapa, M. S., Valenti, J. A., et al. 2001, AJ, 121, 1136

Queloz, D. 1995, Symp. Int. Astron. Union, 167, 221

Queloz, D., Allain, S., Mermilliod, J.-C., Bouvier, J., & Mayor, M. 1998, A&A, 335, 183

Queloz, D., Henry, G. W., Sivan, J. P., et al. 2001, A&A, 379, 279

Quast, G., Torres, C., Reza, R., da Silva, L., & Mayor, M. 2000, Proc. Int. Astron. Union, 200, 28P

Raghavan, D., McAlister, H. A., Henry, T. J., et al. 2010, ApJS, 190, 1

Reiners, A., & Basri, G. 2009, ApJ, 705, 1416

Reipurth, B., & Mikkola, S. 2012, Nature, 492, 1476

Ricker, G. R., Winn, J. N., Vanderspek, R., et al. 2015, J. Astron. Telesc. Instrum. Syst., 1, 014003

Riedel, A. R., Finch, C. T., Henry, T. J., et al. 2014, AJ, 147, 85

Rodet, L., Bonnefoy, M., Durkan, S., et al. 2018, A&A, 618, A23

Rodriguez, D. R., Zuckerman, B., Kastner, J. H., et al. 2013, ApJ, 774, 101

Sartoretti, P., Katz, D., Cropper, M., et al. 2018, A&A, 616, A6

Sato, B., Fischer, D. A., Ida, S., et al. 2009, ApJ, 703, 671

Schlieder, J. E., Lépine, S., & Simon, M. 2012, AJ, 144, 109

Schneider, A. C., Shkolnik, E. L., Allers, K. N., et al. 2019, AJ, 157, 234

Scott, D. W. 1979, Biometrika, 66, 605

Shan, Y., Yee, J. C., Bowler, B. P., et al. 2017, ApJ, 846, 93

Shkolnik, E. L., Hebb, L., Liu, M. C., Reid, I. N., & Cameron, A. C. 2010, ApJ, 716, 1522

Shkolnik, E. L., Anglada-Escudé, G., Liu, M. C., et al. 2012, ApJ, 758, 56

Sperauskas, J., Deveikis, V., & Tokovinin, A. 2019, A&A, 626, A31

Stassun, K. G., Oelkers, R. J., Paegert, M., et al. 2019, AJ, 158, 138

Sterzik, M. F., & Tokovinin, A. A. 2002, A&A, 384, 1030

Sturges, H. A. 1926, J. Am. Stat. Assoc., 21, 65

Tobin, J. J., Looney, L. W., Li, Z.-Y., et al. 2016, ApJ, 818, 73

Tokovinin, A. 2014a, AJ, 147, 86

Tokovinin, A. 2014b, AJ, 147, 87

Tokovinin, A. 2016, AJ, 152, 11

Tokovinin, A. 2019, AJ, 158, 222

Tokovinin, A., & Briceno, C. 2020, AJ, 159, 15

Tokovinin, A., & Horch, E. P. 2016, AJ, 152, 116

Tokovinin, A., Thomas, S., Sterzik, M., & Udry, S. 2006, A&A, 450, 681

Torres, G., Stefanik, R. P., Latham, D. W., & Mazeh, T. 1995, ApJ, 452, 870

Torres, C. A. O., Quast, G. R., da Silva, L., et al. 2006, A&A, 460, 695

Torres, C. A. O., Quast, G., Melo, C., & Sterzik, M. 2008, Handbook of Star Forming Regions, 2, 757

VanderPlas, J. T., & Ivezic, Z. 2015, ApJ, 812, 18

Vaytet, N., Audit, E., Chabrier, G., Commerçon, B., & Masson, J. 2012, A&A, 543, A60

Viana Almeida, P., Melo, C., Santos, N. C., et al. 2012, A&A, 539, A62

Webb, R. A., Zuckerman, B., Platais, I., et al. 1999, ApJ, 512, L63

Zhu, Z., Hartmann, L., Nelson, R. P., & Gammie, C. F. 2012, ApJ, 746, 110

Zuckerman, B., Song, I., & Bessell, M. S. 2004, ApJ, 613, L65

Zuckerman, B., Rhee, J. H., Song, I., & Bessell, M. S. 2011, ApJ, 732, 61

Appendix A: Notes on individual sources

A.1. Sources flagged variable in this work

CD-46 644. This target was flagged due to variation in its $v \sin i$ value. The CCF profile is somewhat asymmetric however, the evidence is not strong enough to confirm its spectroscopic binary nature. Therefore, it was rejected as a spectroscopic binary.

HD 17332 A. This target has two UVES observations and no significant radial velocity variation. However, its $v \sin i$ value was calculated to be 13 and 4 km s^{-1} in the two epochs. Closer inspection of the CCF profile shows that the profile is well-fitted. However, given we only have two epochs, we cannot conclude whether this change is due to a companion or inherent variability of the star. Therefore, at this time ,we flag the system as a questionable SB and flag it for further investigation.

CD-56 1032A. This target has two UVES observations produ-cing radial velocity values of 35.99 and 27.75 km/s^{-1}. The target is a relatively fast rotator ($v \sin i \approx 40$ km s^{-1}) but the rotational profile is well-fitted considering its properties. Therefore, we flagged this target as a spectroscopic binary.

CPD-19 878. This target shows variation in radial velocity. However, given we only have four epochs, we cannot conclude whether this change is due to a companion or inherent variability of the star. Therefore, at this time we flag the system as a questionable SB, and flag it for further investigation.

TYC 7627-2190-1. This target shows significant variation in radial velocity from both our observations and those including literature values. Closer inspection of its CCF profile reveals that it is likely a merged double-lined spectroscopic binary.

*V*PXVir.* This is a known single-lined spectroscopic binary with an orbital solution ($P = 216.48 \pm 0.06$ day), presented in Griffin (2010). In this work, when combined with literature values, the system was flagged as variable.

HD 159911. This target was flagged as having high $v \sin i$ variation. Despite it has a high $v \sin i$ value (≈ 58 km s^{-1}) its CCF profile is well fitted and therefore it is flagged as a potential SB1 system.

CD-43 3604. Its CCF profile has two clear peaks at different depths and the centre of the single Gaussian fit moves significantly from epoch to epoch. The target's rotational broadening is poorly constrained due to the merged double-peak nature of the profile. This target is likely a merged double-lined spectroscopic binary.

V 379 Vel, TYC 8594-58-1, HD 37484.* These targets were flagged due to variation in its radial velocity when a literature value was included. Given that the variation come only for one extra epoch, there is not enough evidence to establish the origin of this variation. Therefore, these targets are rejected from the category of a spectroscopic binary.

2MASS J12203437-7539286. This target only has three observations (two presented here, the other from Torres et al. 2006). However, given its low $v \sin i$ value (≈ 8 km s^{-1}) the difference in radial velocities (0.6 and 4.8 km s^{-1}) is significant.

HD 129496. This target was initially flagged as having potentially variable radial velocity, however it has a very high $v \sin i$ value (≈ 67 km s^{-1}). Its CCF profile is poorly fitted and, therefore, it is rejected from the category of a spectroscopic binary.

CD-52 9381. This target has a high $v \sin i$ value (≈ 40 km s^{-1}) and was flagged due to radial velocity variation ($\sigma_{\rm RV} = 2.75$ km s^{-1}). A closer inspection of its CCF reveals that the profile is asymmetric however, there are not two distinguishable peaks. At this time we reject this target from the category of a spectroscopic binary.

*V*AFLep.* This target was flagged due to variation in its $v \sin i$ value from three measurements. The CCF profile is somewhat asymmetric however, the evidence is not strong enough to confirm its spectroscopic binary nature. Therefore, it was rejected from the category of a spectroscopic binary.

HD 139084. This is a known single-lined spectroscopic and close visual binary. The orbital solution of this system was recently presented in Nielsen et al. (2016). The period of the system is 4.576 yr, placing it at the limit of detectability; see Fig. 8.

HD 139084 B. This target is a fast rotator ($v \sin i \geq 50$ km s^{-1}) and only has two observations (one presented here and other from Torres et al. 2006). For that reason, there is not enough evidence to establish the origin of the variation. Therefore, this target is rejected from the category of a spectroscopic binary.

HD 164249 B. This target was flagged for potential variable $v \sin i$ values. However its CCF profiles are poorly fitted and therefore it was rejected from the category of a spectroscopic binary.

CD-31 16041. This target was flagged due to variation in its $v \sin i$ value from three measurements. The CCF profile is somewhat asymmetric however, the evidence is not strong enough to confirm its spectroscopic binary nature. Therefore, it was rejected from the category of a spectroscopic binary.

*V*PZTel.* This target was flagged due to variation in its $v \sin i$ value. However, it is a very fast rotator ($v \sin i$ 64 km s^{-1}) and its CCF profile is poorly fitted, there it was rejected from the category of a spectroscopic binary.

HD 191089. From our measurements alone, this target would not be flagged as variable. However, with the inclusion of literature values its radial velocity significantly changes. There are two separate measurements (Gontcharov (2006): -5.9 km s^{-1} and Desidera et al. (2015): -6.4 km s^{-1}). The values calculated from our three UVES observations are -12.18, -12.14, and -11.24 km s^{-1}. In the analysis by Grandjean et al. (2020), this source was flagged as a variable due to stellar pulsations. Therefore at this time we flag the system as a questionable SB and flag it for further investigation.

HD 199143. This target is a fast rotator and has been flagged for both variable $v \sin i$ value and radial velocity. The value calculated in this work is $v \sin i \approx 58$ km s^{-1}, compared to that of Torres et al. (2006), 128 km s^{-1}. A closer inspection of its CCF shows that our fit of rotational broadening is most likely underestimated due to the velocity span of the CCF fit ($-180 - +180$ km s^{-1}). Therefore. the value of 58 km s^{-1} should be treated as a conservative lower limit. Additionally the profile is extremely noisy and poorly fitted by both a Gaussian for its radial velocity value and the rotational broadening profiles. Given these limitations the system was rejected from the category of a spectroscopic binary.

*cEri. This target is a very fast rotator ($v \sin i \approx 57$ km s^{-1}). Additionally, its CCF is very noisy and poorly fitted. Therefore, it is likely that the apparent radial velocity variation is not physical and the result of a poorly constrained profile. This system is rejected from the category of a spectroscopic binary.

GJ 3305. Given its low $v \sin i$ value (≈ 5 km s^{-1}) its radial velocity variation ($\sigma_{RV} \approx 1.6$ km s^{-1}) is well above the threshold for identifying it as a spectroscopic binary.

HD 22213. This target has two UVES observations producing radial velocity values of 8.13 and 14.41 km s^{-1}. The target is a relatively fast rotator ($v \sin i \approx 41$ km s^{-1}) but the rotational profile is well fitted considering. Therefore, we flagged this target as a spectroscopic binary.

*V*AGLep.* This target has three UVES observations and no significant radial velocity variation. However, its $v \sin i$ value was calculated to be $\sim$23 and 33 km s^{-1} between the three epochs. Closer inspection of the CCF profile shows that firstly, for a relatively fast rotator the profile is well fitted. However, the shape changes significantly between the two epochs (the bisector slope, curvature and bisector inverse slope change dramatically). However, given we only have two epochs we cannot conclude whether this change is due to a companion or inherent variability of the star. Therefore at this time we flag the system as a questionable SB and flag it for further investigation.

HD 21997. This target was flagged as having variable $v \sin i$, however, given the associated uncertainty and high $v \sin i$ value this variation is not significant.

CD-44 753. This target were flagged due to variation in its radial velocity when a literature value was included. Given that the variation come only for one extra epoch, there is not enough evidence to establish the origin of this variation. Therefore, this targets is rejected as a spectroscopic binary for the moment.

HD 104467. This target was flagged due to significant radial velocity variation. The $v \sin i$ value of the target is ≈ 25 km s^{-1}, and the profile is well fitted. Therefore, this system is flagged as a spectroscopic binary.

2MASS J12020369-7853012. This target was flagged due to significant radial velocity variation. The $v \sin i$ value of the target is ≈ 15 km s^{-1}, and the profile is well fitted. This target was previously flagged as a single-lined spectroscopic binary in Elliott et al. (2014). Therefore this system is flagged as a spectroscopic binary.

BD-20 1111. We have three UVES observations of this target and it has been flagged as having a variable $v \sin i$ value. The shape of the profile significantly changes between two epochs, resulting in the different $v \sin i$ values of 25 and 15 km s^{-1}. Given that we only have three epochs at present, we cannot assess whether this asymmetry is a result of the star's changing surface or of a physically bound companion. Therefore at this time we flag the target as a questionable SB system.

CD-66 395. This target is a very fast rotator ($v \sin i \approx$ 60 km s^{-1}). Additionally, its CCF is very noisy and poorly fitted. Therefore, it is likely that the apparent radial velocity variation is not physical and the result of a poorly constrained profile. This system is rejected as a spectroscopic binary.

BD-184452A. This target only has two $v \sin i$ observations from Torres et al. (2006) and one RV value from *Gaia* DR2. Therefore is not enough evidence yet to establish the origin of the variation. At this time we flag the target as a questionable SB system.

GSC 08057-00342. This target has three radial velocity values in the literature from Rodriguez et al. (2013), Malo et al. (2014), and Kraus et al. (2014). Given its low $v \sin i$ value (≈ 5 km s^{-1}) its large radial velocity variation ($\sigma_{RV} \approx 5$ km s^{-1})

is well above the threshold for identifying it as a spectroscopic binary. This object was also independently identified as a SB by Flagg et al. (2020).

HD 17250. This target has three RV from UVES observations and two from the literature (Gontcharov 2006; Gaia Collaboration 2018). This object is the main star of a quadruple system with two visual companions and was flagged as an SB by (Tokovinin & Horch 2016).

2MASS J04470041-5134405, UCAC3 33-129092, UCAC4 110-129613. These targets only has two observations (one from GDR2 and other from Kraus et al. 2014). There is not enough evidence yet to establish the origin of the variation. Therefore, these target are rejected as a spectroscopic binary.

CD-53 544. This target was flagged due to variation in RV and $v \sin i$ values. The CCF profile is somewhat asymmetric however the evidence is not strong enough to confirm its spectroscopic binary nature.

TYC8098-414-1. There are six available radial velocity measurements for this system. Five of these six measurements would give an RV $\sim$19.60 km s^{-1}, which would not be flagged as SB candidate. However, the inclusion of one value from Kraus et al. (2014) of -1.60 km s^{-1} makes the apparent variation significant. It is difficult to assess these individual values given the available information. At this time, the system is flagged as a potential SB for further investigation.

HD 207575. This target shows variation in radial velocity and $v \sin i$ value. The CCF profile shows that the shape change between the epochs (the bisector slope, curvature and bisector inverse slope). However, given we only have five epochs we cannot conclude whether this change is due to a companion or inherent variability of the star. Recently, Grandjean et al. (2020) flag this source as a variable due to pulsations from HARPS observations. Therefore, this target is rejected as a spectroscopic binary.

HD 207964. This targets only has three observations (one from GDR2 and two from our work). Given that there is not enough evidence to establish the origin of the variation, this target is rejected from the category of a spectroscopic binary.

TYC 9344-293-1. This object has a variable number of $v \sin i$ values. The values are 61 km s^{-1} (Torres et al. 2006), 59.5, 65.4 and 67.5 km s^{-1} (Malo et al. 2014) and 55, 55, and 58 km s^{-1} (this work). The most different was the value of 33.1 km s^{-1} published in Kraus et al. (2014). This system was tagged as a rotational variable but for the moment, it is rejected from the category of a spectroscopic binary.

UCAC3 92-4597. This target was previously flagged as a SB in Malo et al. (2014). In this work, the system was flagged as a variable using the literature values.

CD-30 3394, CD-30 3394B. These objects was flagged due to RV variation. The CCF profile shows that the shape change between the epochs (the bisector slope, curvature, and bisector inverse slope). However, given we only have four epochs we cannot conclude whether this change is due to a companion or inherent variability of the star. At this time, the systems are flagged as a potential SBs for further investigation.

HD 3221. This target is a very fast rotator ($v \sin i \geq$ 68 km s^{-1}) and its profile is extremely noisy and poorly fitted. For that reason the radial velocity variation is likely to be nonphysical. Therefore, this target is rejected from the category of a spectroscopic binary.

SCRJ0103-5515. This target was previously flagged as a double or multiple star in WDS. In this work, the system was flagged as a variable using the literature values from Malo et al. (2014) and Kraus et al. (2014).

V* CE Ant . This target was flagged due to variation in its $v \sin i$ value from our measurements. The CCF profile is somewhat asymmetric, however, the evidence is not strong enough to confirm its spectroscopic binary nature. Therefore, it was rejected from the category of a spectroscopic binary.

TWA23. This target has 16 individual radial velocity measurements (the majority from Bailey et al. 2012) and shows significant radial velocity variation. Although we only have one observation, from UVES, the profile is consistent as resulting from a merged SB2 system. There is a significant asymmetry at approximately half the depth of the profile, causing a large bisector slope. Therefore this target is flagged as an SB2 system.

V* AO Men. This target was flagged due to variation in its radial velocity when a *Gaia* DR2 value was included. Given that the variation come only for one extra epoch, there is not enough evidence to establish the origin of this variation. On the other hand, Grandjean et al. (2020) estimated that the variation was due to stellar activity (spots). Therefore, this target is rejected from the category of a spectroscopic binary.

HD 984. This target was flagged due to variation in its radial velocity when a *Gaia* DR2 value was included. Johnson-Groh et al. (2017) calculated the orbit of this system as ~70 yr, which is outside outside the region where a visual binary can be detected through radial velocity variation given ~10 yr measurements. Therefore, although this object is a visual binary, it cannot be flagged as a spectroscopic binary.

2MASS J01505688-5844032, UCAC4 137-000439. These targets were flagged due to variation in its radial velocity from two literature values (Kraus et al. 2014; Gaia Collaboration 2018). Shan et al. (2017) did not find sign of companion from adaptive optics observations conducted on the 6.5 m Magellan Clay Telescope for these objects. UCAC4 137-000439 was noted as potential tight binary in Janson et al. (2017) with an estimated separation of ~0.01″. 2MASS J01505688-5844032 is rejected from the category of a spectroscopic binary for the moment and UCAC4 137-000439 is flagged as a potential SB for further investigation.

2MASS J12560830-6926539. This target only has two observations (one from Torres et al. 2006 and another from *Gaia* DR2). Elliott et al. (2015) probed binarity in this object by high-resolution imaging with an estimated angular separation of 0.1″, physical separation of 13.1 au and a mass ratio of 0.55. This object is at the boundaries of the region where a visual binary can be detected through radial velocity variation given ~10 yr measurements. At this time, we flag the target as a questionable SB system.

Smethells 165. This target was previously flagged as a double or multiple star in WDS. In this work, the system was flagged as a variable using the $v \sin i$ values from literature. The variation came from one $v \sin i$ measurement from Kraus et al. (2014). At this time. we flag the target as a potential SB for further investigation.

A.2. Sources previously flagged as spectroscopic multiple systems not recovered in this work

CD-29 4446. This is a known binary system with an orbital solution presented in Rodet et al. (2018). In this work, the system was flagged as a variable using the literature values.

V* V1005 Ori. This target was flagged as an SB1 system in Elliott et al. (2014). The compilation of further radial velocities do not show significant radial velocity variation caused by a companion.

HD 98800A. Torres et al. (1995) calculated the orbit of this SB1 system as 262 day. In the results presented here we only have two radial velocity values which are four days apart and, therefore, did not detect any significant change in velocity. This is one of the few clear spectroscopic systems missed by our analysis.

CD-33 7795. This target is a known triple system with companions at ≈0.06″ (Macintosh et al. 2001) and 2″ (Webb et al. 1999). Konopacky et al. (2007) calculated the orbit of the inner system as 5.94 ± 0.09 yr, which puts it in the approximate region where a visual binary can be detected through radial velocity variation given ~10 yr measurements. However, this object is a fast rotator ($v \sin i \approx 50$ km s^{-1}) and only has two epochs of radial velocity data which do not show significant variation. Therefore, although this object is a visual binary it cannot be flagged as a spectroscopic binary.

HD 13183. This target was flagged as a potential SB1 system in the CORAVEL database (Nordstrom et al. 1996). Furthermore, Cutispoto et al. (2002) found evidence for significant radial velocity variation. From our compilation of values, this system does not exhibit significant variation given its rotational velocity ($v \sin i \approx 24$ km s^{-1}); however, it does have an asymmetrical CCF profile. Given the previous notes in multiple other works, this system is flagged as a spectroscopic binary.

A.3. Double- and triple-lined spectroscopic binaries

Double- and triple-lined spectroscopic multiple systems can be identified from a single epoch of data and are essentially confirmed as multiple systems with one detection. For that reason, the notes below on each system are brief, with references to their original discovery where applicable.

HD 67945. This target was flagged as a potential SB2 system in Torres et al. (2006). However, given its extremely fast rotation $v \sin i \geq 58$ km s^{-1} and extremely noisy CCF profile we do not find sufficient evidence to confirm that. Additionally it does not have significant radial velocity variation. Therefore, it was rejected from the category of a spectroscopic binary.

HD 155177. There are three individual radial velocity values for this target with uncertainties <3 km s^{-1}, two of which are calculated in this work. Both the shape (b_b, c_b and *BIS*) and the peak of the CCF profile change significantly across the two observations. Therefore, this system is flagged as a spectroscopic binary.

GSC 06513-00291. Malo et al. (2014) flag this system as an SB2 and quote values of 12.1, 21.6 and 2.4 for $v \sin i$ of this target from three observations. Interestingly the RV values from the three epochs 22 and 23.9 and 22.8 do not vary significantly. This target has a companion at ≈0.1″. Therefore, it is likely an SB3 system. The companion at 0.1″ (3 au using a trigonometric distance of 29.4 pc, Riedel et al. 2014) would have a period

>1000 day. Such a period would not typically induce a large RV difference unless the orbit was extremely eccentric. This system is therefore flagged as an SB3.

V4046 Sgr. This target is a well-known SB2 system, the orbital solution was presented in Quast et al. (2000). We recover both components of this system in all CCF profiles.

LP 476-207 A. This is a known SB2 system whose orbital solution was presented in Delfosse et al. (1999). We recover both components of this system in all CCF profiles.

Barta 161 12. We do not have our own observations of this target and therefore cannot further investigate the spectroscopic binary-nature of this object with our measurements. However, Malo et al. (2014) reported this target as an SB2 system. There are multiple radial velocity measurement that show apparent variation, however, it was not recovered in our analysis as the majority of measurements have uncertainties larger than 3 km s^{-1}. This target is therefore flagged as a spectroscopic binary.

HD 217379A. This is a previously discovered SB3 system (Elliott et al. 2014). More recently, Tokovinin (2016) presented an orbital solution for both the inner and outer system. We recover all three components of this system in our CCF profiles.

TWA 3A. This target was flagged as an SB2 system in Malo et al. (2014) We do not have further observations from UVES, FEROS or HARPS. However, from our compilation of radial velocities this system has significant radial velocity variation.

UCAC3 112-6119, UCAC3 92-4597. Kraus et al. (2014) flagged these two targets as an SB2 systems. We do not have further observations from UVES, FEROS, or HARPS. However, from our compilation of radial velocities these systems have significant radial velocity variation.

HD 309751, HD 33999. These two systems were previously reported in Elliott et al. (2014) and recovered in this analysis.

HD 36329. This SB2 system was previously reported in Torres et al. (2006) and recovered in this analysis.

TYC 8098-414-1. Kraus et al. (2014) noted this target as an SB2 system, however, we do not recover the component in our analysis. Most likely the companion is not detected as its flux ratio is to low in our optical spectra. Malo et al. (2014) also noted that their $v \sin i$ value did not agree with the literature values and mentioned that this could be an unresolved spectroscopic binary. Given this information the system is flagged as an SB2 in our analysis.

HD 199058. Chauvin et al. (2015) noted this object as a binary or multiple system. In this work we flagged this target as an SB2.

TYC 6872-1011-1, BD-20 951, GSC 08077-01788, UCAC3 116-474938, V V1215 Cen, HD 36329.* To the best of our knowledge these systems have not previously been reported in the literature. All are newly discovered SB2 systems.

Appendix B: Measurements of *v sin i*

B.1. Calibrating using CCF width

In the case of slow rotators ($v \sin i \lesssim 20$ km s^{-1}), there is a significant contribution to the width ($\sigma_{\rm obs}$) of the cross correlation function (CCF) from non-rotation related broadening mechanisms which can either be inherent to the star (effective temperature and turbulence) or from the instrument that is used for the
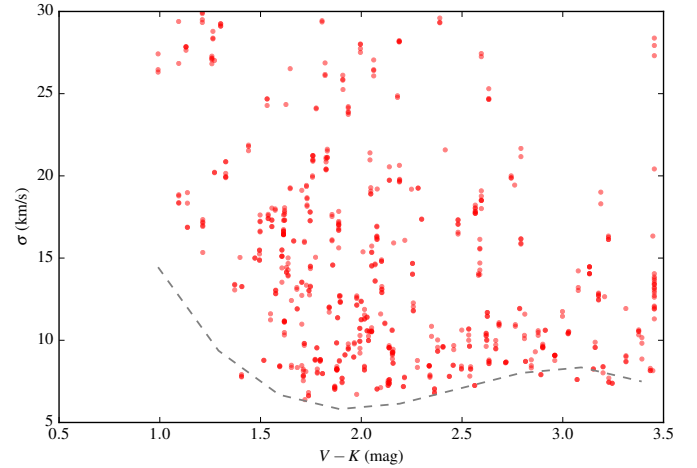

Fig. B.1. $V - K$ colour versus σ (the observed width of the CCF profile) for all individual UVES observations. The dotted line represents a polynomial fitted to the lower envelope of these measurements.

observation. The width of the CCF profile is described by:

$$\sigma_{\rm obs}^2 = \sigma_{\rm rot}^2 - \sigma_0^2, \tag{B.1}$$

where $\sigma_{\rm obs}$ is the width of the resultant CCF profile, $\sigma_{\rm rot}$ is the rotational broadening of the star and σ_0 is the width of a non-rotating star, which can be very well expressed as a function of colour.

Beyond ≈ 20 km s^{-1} the width of the CCF profile is dominated by the rotation of the star and therefore these effects become small or negligible. We note that within our sample of objects there are very few measurements with FEROS or HARPS with $v \sin i$ values ≥ 20 km s^{-1}.

The $v \sin i$ value can be expressed as (Queloz et al. 1998):

$$v \sin i = A \sqrt{\sigma_{\rm obs}^2 - \sigma_0^2}, \tag{B.2}$$

where A is the coupling constant, calibrating one set of CCF measurements to previously calibrated $v \sin i$ values.

Firstly, to determine the value of σ_0, we computed the lower envelope of points in a $V - K$ versus $\sigma_{\rm obs}$ diagram; see Fig. B.1 for an example using UVES observations. The envelope was fitted with a polynomial and is shown as the dotted line. This is similar to the technique used in Melo et al. (2001) and Boisse et al. (2010). We used this σ_0 value for each star with its respective $V - K$ colour and found the slope (and offset) between published $v \sin i$ values and our calculated $A \sqrt{\sigma_{\rm obs}^2 - \sigma_0^2}$ values. We note that in this analysis we used CCF profiles with low fit residuals in order to better constrain the results.

Figure B.2 shows the resultant relation for observations using UVES. We have highlighted three regions of the Fig. to guide the reader's eye. Below ≈ 6 km s^{-1}, in the case of UVES, $\sigma_0 \approx \sigma_{\rm obs}$ and, therefore, this is our reliable lower limit on $v \sin i$ values. Between ≈ 6–20 km s^{-1} the 1:1 linear relation sufficiently describes the majority of our data.

Figure B.2 shows that, at least in the case of UVES observations, this calibration is relatively successful as the literature $v \sin i$ values match the $A \sqrt{\sigma_{\rm obs}^2 - \sigma_0^2}$ value. However, in the case of FEROS and HARPS we were unable to perform the same analysis successfully. Due to the smaller number of objects an accurate calculation of σ_0 was severely inhibited. With this in mind, below we outline an alternative approach to $v \sin i$ calculation.

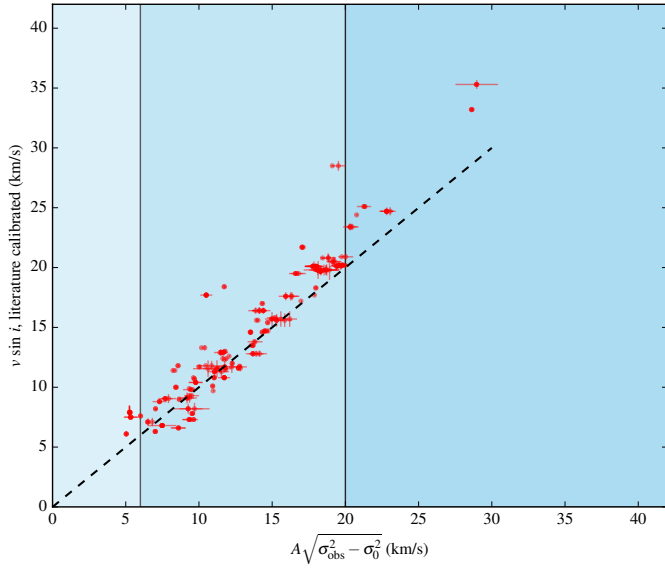**Fig. B.2.** $A\sqrt{\sigma_{obs}^2 - \sigma_0^2}$ versus literature $v \sin i$ values for UVES observations. Three regions are highlighted. From left to right: our lower limit on reliable $v \sin i$ values (6 km s^{-1}), the intermediate range (6–20 km s^{-1}) where the 1:1 relation should hold and the fast rotator range (>20 km s^{-1}). The dotted line represents the 1:1 relation between the two sets of values.
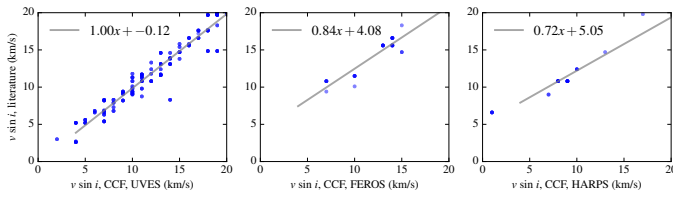

Fig. B.3. $v \sin i$ values from fitted rotational profiles versus literature $v \sin i$ values. The *left, middle and right panels* show measurements for UVES, FEROS and HARPS observations. The linear relation ($y = mx + c$) is shown for each set of measurements.
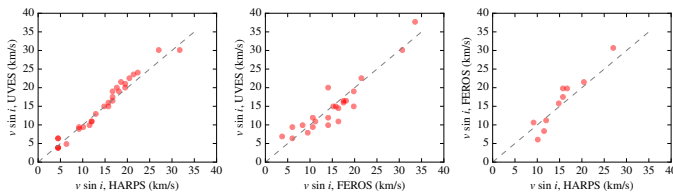

Fig. B.4. $v \sin i$ values calculated in this work for each pair of instruments. *Left, middle and right panels* are HARPS versus UVES, FEROS versus UVES and HARPS versus FEROS, respectively. The 1:1 relation in each case is plotted as the dotted line.

B.2. Calibrating using rotational profiles

We directly compared our calculated values using rotational profiles to published values. We used $v \sin i$ with published uncertainties <3 km s^{-1} in this analysis. Figure B.3 shows the results for UVES, FEROS and HARPS in the left, middle and right panels, respectively. A linear relation ($y = mx + c$) was fitted to each set of points and was used to calibrate our values.

To verify this relationship we performed an internal check by comparing $v \sin i$ values for objects that were observed with at least two of the three instruments. Figure B.4 shows the results of this comparison for each pair of instruments. Given typi-
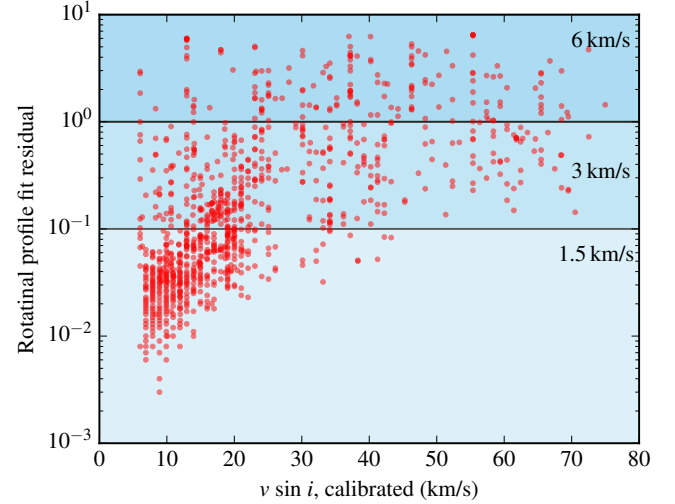
Fig. B.5. Rotational profile fit residual as a function of calibrated $v \sin i$ values. The $v \sin i$ uncertainties value is defined depending on the range of fit residual values.

cal uncertainties on $v \sin i$ values are 1–2 km s^{-1} (Melo et al. 2001; Malo et al. 2014) the resultant 1:1 relationships adequately describe our data. The advantage of this calibration technique is that the linear relation can be applied to all stars in our sample. However, in the case of the technique described in Appendix B.1, a $V - K$ value is needed and some stars in our sample do not have reliable V magnitudes. Additionally, our stars cover the age range $\approx$5–150 Myr and therefore can be at very different evolutionary stages, which could hinder a robust σ_0 calculation.

B.3. v sin i lower limit

From our calibration of $v \sin i$ values described in the previous section, we arrive at lower limits of 0.83, 4.47 and 8.36 km s^{-1} using a star rotating with a projected rotational velocity of 1 km s^{-1} for UVES, HARPS and FEROS, respectively. However, as highlighted in Appendix B.1, we take a more realistic lower limit on $v \sin i$ values for UVES is 6 km s^{-1}, where $\sigma_0 \approx \sigma_{obs}$.

B.4. Limitations on v sin i measurements of extremely fast rotators

In the case of very large rotational broadening ($v \sin i \geq$ 60 km s^{-1}), some stars' $v \sin i$ values can be underestimated. This is due to the width of the profile approaching the width of the velocity span used in the CCF calculation. This causes a lack of continuum and when the profile is fitted the outer wings of the profile can be wrongly ignored. For fast rotators in our sample ($v \sin i \geq$ 50 km s^{-1}), we reran our CCF calculation using a wider velocity window of -250 to $+250$ km s^{-1}. Even with this broader window some star's CCF profile widths were still underestimated. In these cases, we use our calculated value as a lower limit.

B.5. Measurement uncertainties on v sin i values

We compared our calibrated $v \sin i$ values with the fitted linear relation (see Appendix B.2) and calculate the quadratic sum of the error as tracer of uncertainties. We set three uncertainties values based on three order of magnitude from residuals. These

values were selected from the mean uncertainty value from the errors between the calibrated $v \sin i$ and the fitted linear relation on each range of profile fit residuals (see Fig. B.5).

Appendix C: Sensitivity maps

Average detection probability maps (contours from red, 100%, to white, 0%) computed for the population of binaries described in Sect. 7. Detected spectroscopic companions (white stars) and visual binaries (black crosses) in the physical separation versus mass ratio. The solid, dashed, and dash-dotted lines encompass areas with detection probabilities ≥90%, 50% and 10 %, respectively. For THA and BPC association see Fig. 8.
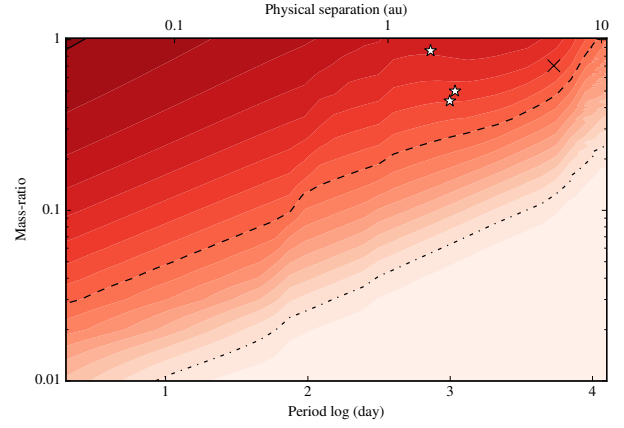

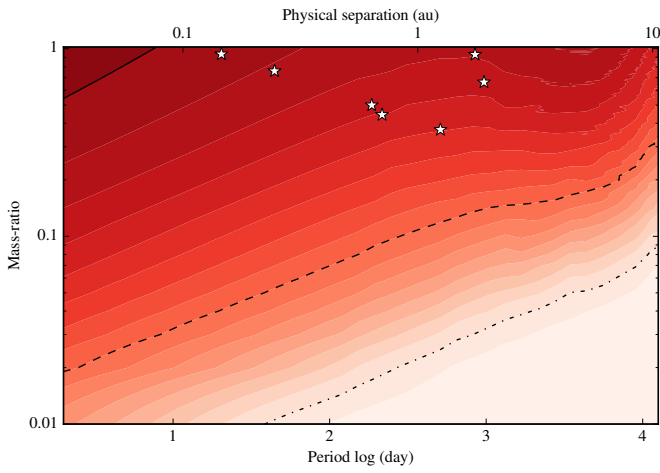**Fig. C.3.** Average detection probabilities for COL association.

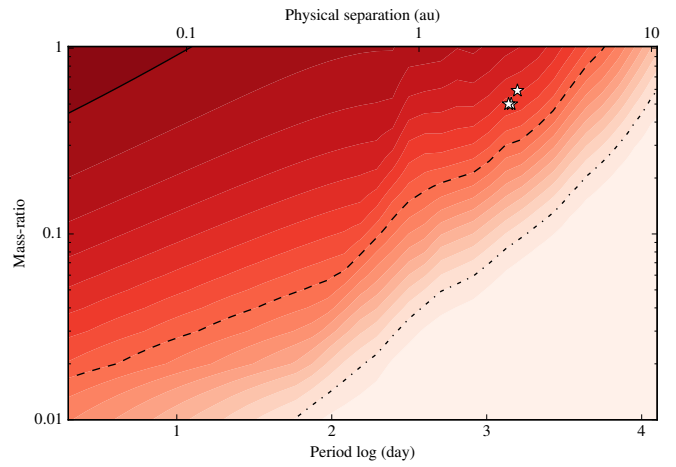**Fig. C.1.** Average detection probabilities for ABD association.

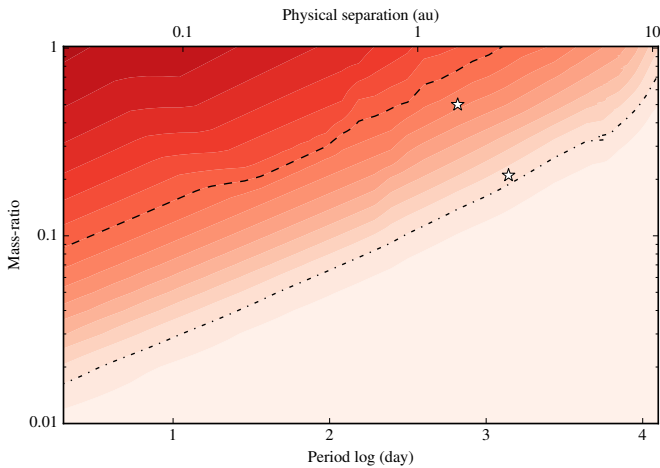**Fig. C.4.** Average detection probabilities for ECH association.

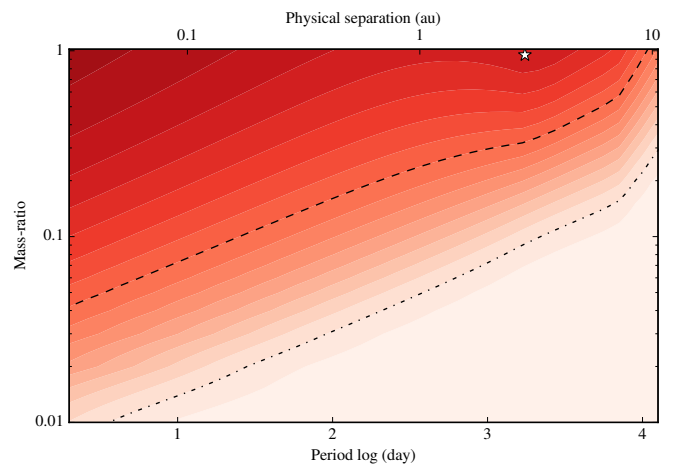**Fig. C.2.** Average detection probabilities for ARG association.

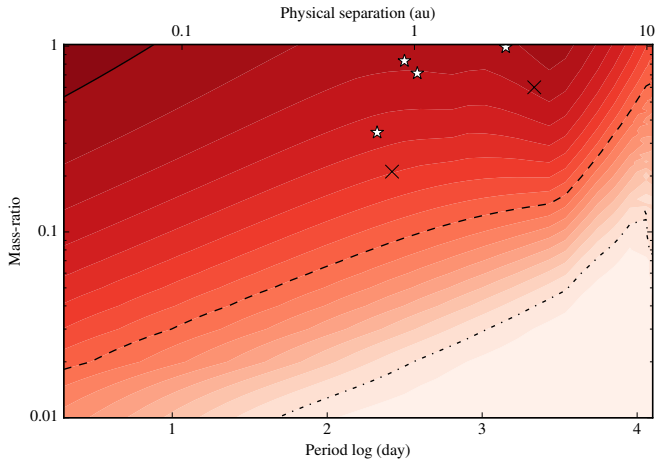
Fig. C.5. Average detection probabilities for OCT association.

Fig. C.6. Average detection probabilities for TWA association.

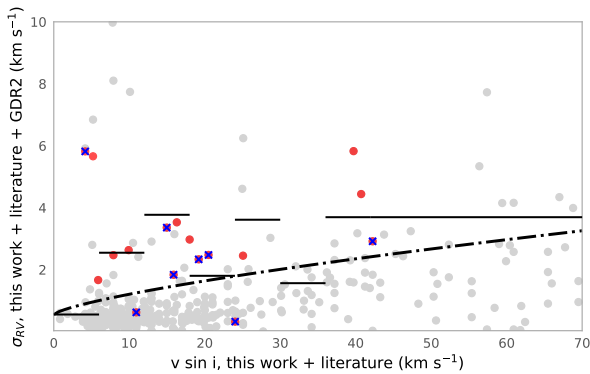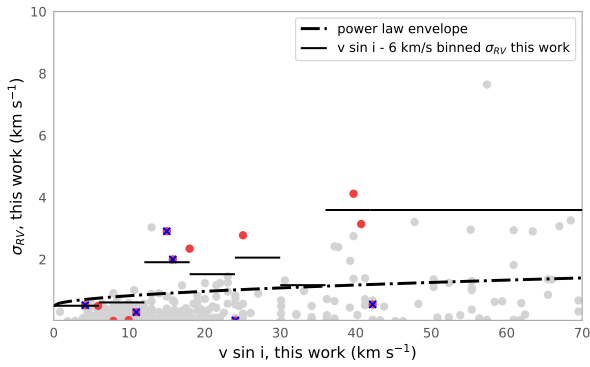## Appendix D: SB1 systems identified in this work

Fig. D.1. *Upper panel*: standard deviation in RV as a function of $v \sin i$ for measurements calculated in this work. The 3σ value from binning in $6 \, \mathrm{km \, s^{-1}}$ bins are represented by the solid lines. The power law envelope is represented by dash-dotted line. The SB1s identified in this work are plotted as a red dots and the previously identified SB1s from literature are represented as a blue crosses. *Bottom panel*: same as upper panel but including values from literature and *Gaia* DR2. Some SB1 were confirmed only when literature values were included (red dots under the 3σ envelope in *upper panel*). Details on each candidate can be found in Appendix A.
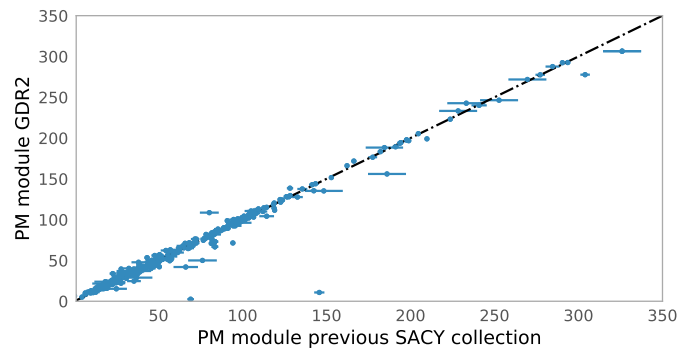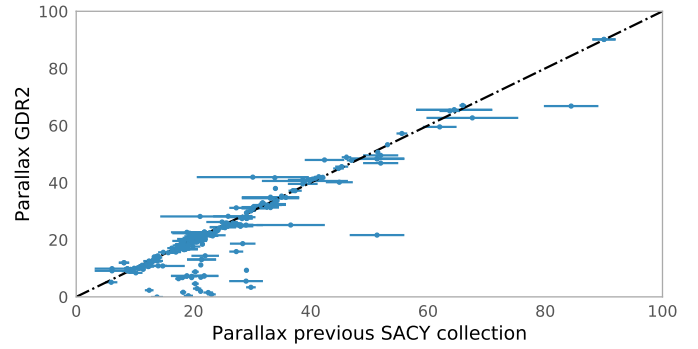
Appendix E: *Gaia* DR2

Fig. E.1. Possible mismatched results was visually inspected and cross-checked to avoid false positives. The dotted-dashed line represent the 1:1 relation.

Example of the sanity checks performed regarding the correct identification of the *Gaia* DR2 counterparts to the SACY members.

Appendix F: Rotational periods from light curves

Fig. F.2. Output figure for GSC 07396-00759 from the package `tpfplotter` (Aller et al. 2020). We count the number of *Gaia* sources within a ΔG mag ≤ 5 of the science target that fall in the pipeline aperture of TESS and save the minimum ΔG mag value to assess the quality of the rotational period.

In Fig. F.1, we show an example of the TESS light curve folded to the period estimated in this work for GSC 07396-00759. The lower panel shows the residuals obtained after subtraction of the binned and smoothed phased light curve to be used to asses the reliability of the period. We can see that despite possible flares in the data-set, our procedure offers a simple but robust diagnostic. On the other hand, as it is evident from Fig. F.2, the aperture used to derive the TESS light curve is contaminated by similar brightness objects and, therefore, we cannot assure that the reported value is the rotational period of this particular source.
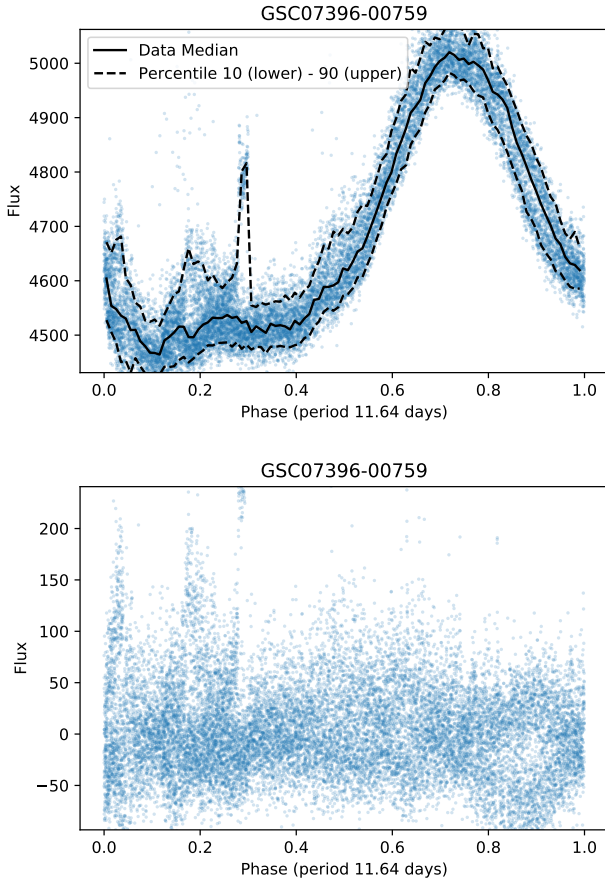
Fig. F.1. *Upper panel:* phased light curve for GSC 07396-00759. The solid line represent the median calculated by binning the phased curve in 100 bins. The MAD for the phased curve for this object is 652.67. *Bottom panel:* residuals from subtracting light curve values from the "median model" (solid line). The MAD of the residuals is 121.84.
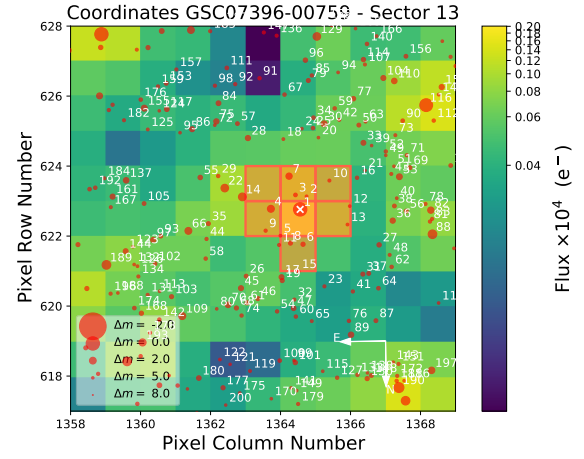
Appendix G: Individual and summary tables

Table G.1. Individual radial velocity values calculated in this work and compiled from the literature/*Gaia* DR2 (first 10 rows).

SIMBAD ID	RA J2000 (deg)	Dec J2000 (deg)	RV	RV err	MJD	BIS	b_b	c_b	Instrument	Ref.
BD-202977	144.964005	−21.571400	18.87	0.532750	53906	−0.404	−8.353	−0.150	FEROS	ZF20
BD-202977	144.964005	−21.571400	17.73	0.532750	54240.1	−0.103	−2.283	−0.138	UVES	ZF20
BD-202977	144.964005	−21.571400	17.75	0.532750	54240.1	−0.089	−1.893	−0.133	UVES	ZF20
HD 99827	171.324005	−84.954399	20.01	1.390170	54906.3	−0.430	−73.848	−0.676	UVES	ZF20
HD 99827	171.324005	−84.954399	19.94	1.390170	54906.3	−0.747	−60.319	−0.830	UVES	ZF20
HD 99827	171.324005	−84.954399	16.30	1.390170	55371.1	0.894	7.246	−1.184	UVES	ZF20
HD 99827	171.324005	−84.954399	19.42	1.390170	56734.3	1.609	81.204	−0.746	UVES	ZF20
HD 99827	171.324005	−84.954399	19.55	1.390170	56748.1	0.810	9.514	−2.268	UVES	ZF20
CD-691055	194.606995	−70.480301	13.70	0.894763	54577	−1.860	−90.714	4.322	FEROS	ZF20
CD-691055	194.606995	−70.480301	12.53	0.894763	55978.4	1.439	13.629	2.944	UVES	ZF20

Notes. The full table (2048 RV values) is published at the CDS in the machine-readable format. The high order features (BIS, b_b, c_b) are available for all our CCF calculations. The MJD and instrument information is not available for all rows in the table, more details in Sect. 2.
References. ZF20: this work or updated value of Elliott et al. (2014), SC12: Schlieder et al. (2012), SH12: Shkolnik et al. (2012), TO06: Torres et al. (2006), LO06: Lopez-Santiago et al. (2006), RO13: Rodriguez et al. (2013), MA10: Maldonado et al. (2010), MO13: Moór et al. (2013), RE09: Reiners & Basri (2009), GO06: Gontcharov (2006), MA14: Malo et al. (2014), KR14: Kraus et al. (2014), MO01b: Montes et al. (2001), MO02: Mochnacki et al. (2002), BA12: Bailey et al. (2012), DE15: Desidera et al. (2015) and GDR2: *Gaia* DR2, Gaia Collaboration (2018).

Table G.2. Individual rotational velocity values calculated in this work and compiled from literature (first 10 rows).

SIMBAD ID	RA J2000 (deg)	Dec J2000 (deg)	$v \sin i$	$v \sin i$ err	Ref.
BD-202977	144.964005	−21.571400	13.49	1.5	ZF20
BD-202977	144.964005	−21.571400	9.92	1.5	ZF20
BD-202977	144.964005	−21.571400	9.92	1.5	ZF20
HD 99827	171.324005	−84.954399	41.23	3.0	ZF20
HD 99827	171.324005	−84.954399	40.22	3.0	ZF20
HD 99827	171.324005	−84.954399	39.21	3.0	ZF20
HD 99827	171.324005	−84.954399	41.23	3.0	ZF20
HD 99827	171.324005	−84.954399	41.23	6.0	ZF20
CD-691055	194.606995	−70.480301	15.20	6.0	ZF20
CD-691055	194.606995	−70.480301	28.10	6.0	ZF20

Notes. The full table (1480 $v \sin i$ values) is published at the CDS in the machine-readable format.
References. ZF20: this work, SC12: Schlieder et al. (2012), TO06: Torres et al. (2006), MA14: Malo et al. (2014), BA12: Bailey et al. (2012) and DE15: Desidera et al. (2015).

Table G.3. Component radial velocity values for SB2 systems estimated in this work.

SIMBAD ID	RA J2000 (deg)	Dec J2000 (deg)	RV1	RV1 err	RV2	RV2 err	MJD
GSC08077-01788	72.970802	−46.791901	−21.2927	1.618303	70.72530	0.694135	56735.1
GSC08077-01788	72.970802	−46.791901	−15.4776	1.312729	65.67440	1.338559	56738.1
HD 199058	313.588013	9.040000	−30.0904	1.000865	−11.77740	1.547928	56828.4
HD 199058	313.588013	9.040000	−24.9204	0.972239	−13.04740	1.352694	56836.3
HD 199058	313.588013	9.040000	−24.5381	0.860092	−15.96410	1.037438	57275.1
HD 199058	313.588013	9.040000	−25.0000	0.904851	−13.90000	1.964319	54783.0
HD 36329	82.350403	−34.515598	23.8599	0.979925	23.85990	0.904718	57271.4
HD 36329	82.350403	−34.515598	−44.8610	1.290879	90.64900	1.382289	57276.4
HD 36329	82.350403	−34.515598	−19.5175	1.143967	68.21940	1.918715	57295.3
HD 51062	103.447998	−43.114201	14.6000	0.912295	38.90000	0.997951	55522.3
HD 99827	171.324005	−84.954399	1.7000	1.269730	33.50000	1.642376	54169.2
UCAC3116-474938	299.011993	−32.121899	−29.8203	1.363111	15.90560	1.102911	57255.3
UCAC3116-474938	299.011993	−32.121899	−66.4405	1.185148	54.73050	1.044546	57272.1
UCAC3116-474938	299.011993	−32.121899	−40.6756	1.003758	28.52240	1.520679	57275.1
UCAC3116-474938	299.011993	−32.121899	−14.4882	1.280286	2.47079	0.857250	57292.2

Table G.4. Summary table of the sample presented in this work.

Label	Units	Description
Simbad ID		Simbad identifier
RA J2000	Degrees	Right ascension at J2000
DEC J2000	Degrees	Declination at J2000
RV_{median} CCF	$km\,s^{-1}$	Median RV from our CCF calculation
σ_{RV} CCF	$km\,s^{-1}$	Standard deviation in RV from our CCF calculation
$v \sin i_{median}$ CCF	$km\,s^{-1}$	Median $v \sin i$ from our CCF calculation
$\sigma_{v \sin i}$ CCF	$km\,s^{-1}$	Standard deviation in $v \sin i$ from our CCF calculation
N_{obs} CCF		Number of observation from our CCF calculation
RV_{median}	$km\,s^{-1}$	Median RV from our work + literature
σ_{RV}	$km\,s^{-1}$	Standard deviation in RV from our work + literature
N_{obs} RV		Number of RV observations from our work + literature
$v \sin i_{median}$	$km\,s^{-1}$	Median $v \sin i$ from our work + literature
$\sigma_{v \sin i}$	$km\,s^{-1}$	Standard deviation in $v \sin i$ from our work + literature
$N_{obs}\, v \sin i$		Number of $v \sin i$ observations from our work + literature
Period	Days	Period from light curves
σ_{Period}	Days	Period uncertainty
FAP		False alarm probability
Phased-MAD		MAD on phased light curve
Residual-MAD		MAD on residuals of phased light curve
P-MAD/R-MAD		Ratio between phased-MAD and residuals-MAD
INSTR.		Instrument that has measured the light curve
TESS sector		TESS sector
TESS/K2 ID		TESS or K2 identifier
$N_{sources}$ TESS		Number of sources in TESS aperture with ΔG mag < 5
$Min_{\Delta G\,mag}$ TESS	mag	Minimum ΔG mag in TESS aperture
LC notes		Light curves notes on the object
LC q_{flag}		Light curve quality flag (Good, Caution or Bad)
Gaia DR2 ID		*Gaia* DR2 source identification
mass	$M_\odot$	Stellar mass
Spt		Spectral type
$SACY_{MG}$		Best MG match from SACY convergence method
$SACY_P$		SACY membership probability
BAN_{MG}		Best MG match from BANYANΣ
BAN_P		BANYANΣ membership probability
Notes		Notes on SB candidates

Notes. This table is only available at the CDS.